

Research Article

Highly refractory harzburgites from the Moa-Baracoa Ophiolitic Massif, Eastern Cuba: Insights into forearc mantle melt-rock interactions

Hui-Chao Rui^a, Jing-Sui Yang^{b,c,*}, Angélica I. Llanes Castro^d, Jian-Ping Zheng^a, Fei Liu^c, Yurisley Valdes Mariño^e, Wei-Wei Wu^{b,c}, Tian Qiu^c

^a School of Earth Sciences, China University of Geosciences, Wuhan 430074, China

^b School of Earth Sciences and Engineering, Nanjing University, Nanjing 210023, China

^c Center for Advanced Research on the Mantle (CARMA), Chinese Academy of Geological Sciences, Beijing 100037, China

^d Department of Petrology and Mineralogy, Institute of Geology and Paleontology, Havana 10200, Cuba

^e High Mining Metallurgic Institute of Moa "Dr. Antonio Nunez Jimenez", Moa 83310, Cuba



ARTICLE INFO

Keywords:

Highly refractory harzburgites
Moa-Baracoa Ophiolite
Melt-rock interaction
Forearc mantle
Eastern Cuba

ABSTRACT

Melt-rock interactions are important for understanding the long-term evolution of the Earth and for addressing various mantle compositions. However, details of the mechanisms and evolution of interactions in supra-subduction zones remain poorly understood. This study presents petrographic and geochemical analyses of the harzburgites from the Moa-Baracoa Ophiolitic Massif, eastern Cuba, to constrain the melt-rock interaction within the lithospheric mantle. The harzburgites preserve pristine microstructures by recording three-stage petrogenetic processes: incongruent melting of orthopyroxene (Opx) in stage I; crystallization of interstitial clinopyroxene (Cpx), spinel (Sp), and base-metal sulfides (BMS) at the expense of Opx in stage II; and re-equilibration characterized by Sp-Cpx symplectite in stage III. The harzburgite compositions are highly refractory with Al₂O₃ (0.21–0.81 wt%) and TiO₂ (~0.04 wt%) and show “U”-shaped rare earth element (REE) patterns and significant LREE and large ion lithophile element (LILE) enrichments. The olivines have an E-type fabric and a narrow range of compositions (Fo = 90.6–91.6). Interstitial Cpx has moderate Mg# (92.1–94.9) and Al₂O₃ (1.06–2.88 wt%) and extremely low TiO₂ contents (<0.03 wt%). Opx and interstitial Cpx have low ΣREE contents (0.09–0.14 ppm and 0.24–0.49 ppm, respectively) and are depleted in LREE and variably enriched in LILE. Spinels possess similar Cr# values (56.7–64.8) but variable Mg# values (37.2–58.4). BMS is primarily dominated by pentlandite, which is partly or completely replaced by magnetite and/or heazlewoodite. Modeling of whole-rock HREE variations suggests that the harzburgites experienced >25% partial melting. Widespread interstitial Cpx and BMS, elevated whole-rock Cu and Pt, and variable LILE enrichment in Opx and Cpx indicate the interaction of the refractory harzburgites with migrating sulfur-saturated, low-silica melts. Melts equilibrated with interstitial Cpx appear to have an affinity for FAB. Mineralogical, chemical, and olivine fabric evidence suggests that the Moa-Baracoa harzburgites originated in a nascent forearc mantle. The harzburgites experienced partial melting facilitated by migrating low-silica melts in stage I. Subsequent interactions with FAB melts at relatively high temperatures precipitated Sp, Cpx, and BMS in stage II. Finally, the re-equilibration of high-temperature/pressure pyroxenes produced Sp-Cpx symplectite as the harzburgites were rapidly emplaced into the lithospheric mantle during subduction initiation.

1. Introduction

Partial melting of the mantle has continuously built the oceanic crust from the Archean to the present day (Furnes et al., 2014; Parkinson and Pearce, 1998). Melts produced by relatively lower pressure partial melting of depleted peridotites likely migrate through porous flow,

giving rise to extensive melt-rock interactions in the upper mantle (Abdullah et al., 2018; Dijkstra et al., 2003; Piccardo et al., 2007; Seyler et al., 2001). Melt-rock interaction refers to a range of processes (e.g., melting, solidification, and re-equilibration (Suhr et al., 2008; Warren, 2016)) that are pervasive beneath spreading centers and persistently modify the abyssal and forearc mantle at varying levels (Basch et al.,

* Corresponding author at: 163 Xianlin Road, Qixia District, Nanjing, Jiangsu Province 210023, China.

E-mail address: yangjsui@163.com (J.-S. Yang).

<https://doi.org/10.1016/j.lithos.2021.106427>

Received 3 February 2021; Received in revised form 6 August 2021; Accepted 6 August 2021

Available online 19 August 2021

0024-4937/© 2021 Elsevier B.V. All rights reserved.

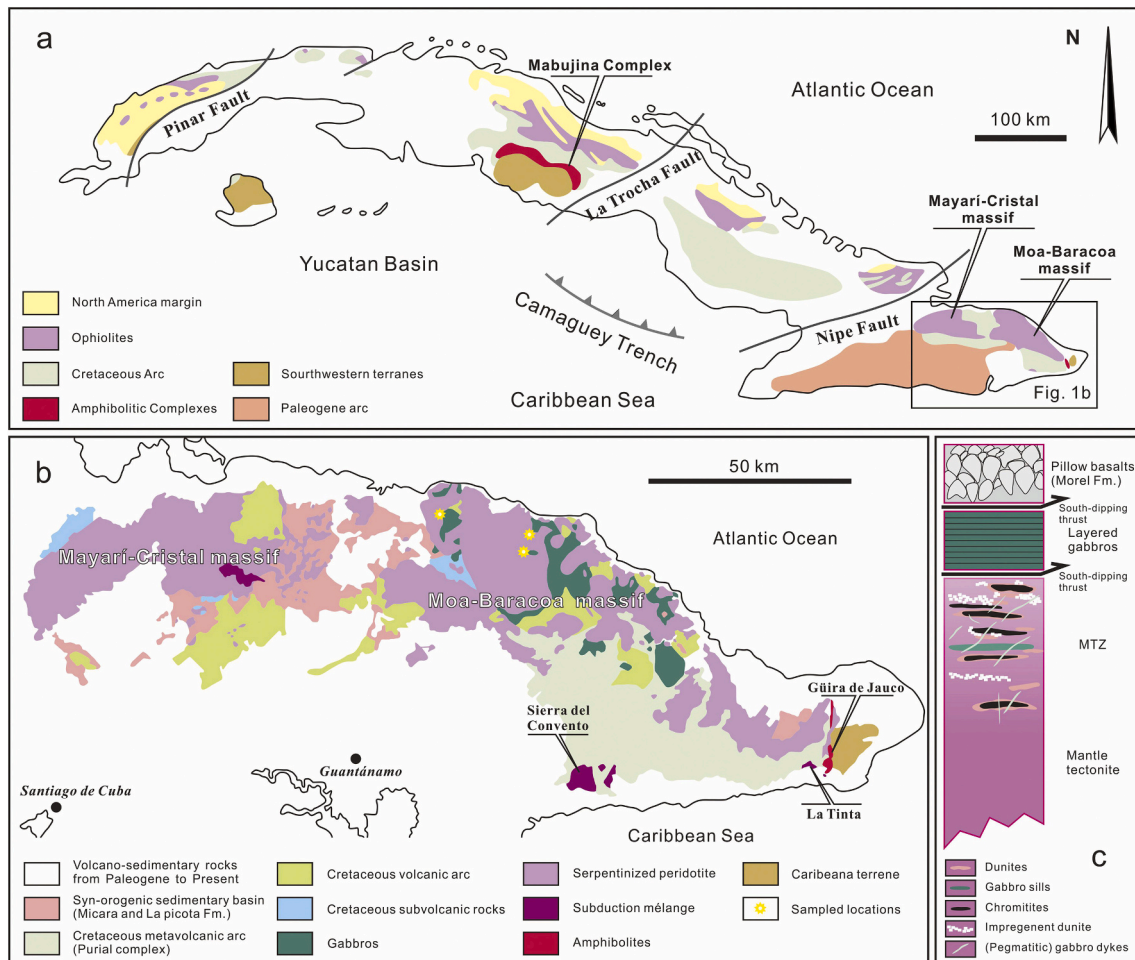


Fig. 1. (a) Generalized geological map of Cuba (after Lázaro et al., 2016); (b) Geological map of eastern Cuba showing the main geological units (after Lázaro et al., 2016); (c) Schematic lithostratigraphic column of the Moa-Baracoa massif (after Proenza et al., 2018).

2019; Seyler et al., 2007; Xu et al., 2021). This interaction leads to a heterogeneous oceanic lithosphere, which is recycled back into the mantle and produces further heterogeneity (Warren, 2016). Thus, melt-rock interaction is critical for understanding the long-term compositional evolution of the Earth and can help determine various mantle compositions (Seyler et al., 2007; Uysal et al., 2012; Xiong et al., 2020).

However, due to the lack of clear chronological microstructure evidence in mantle peridotites, the mechanism and evolution of melt-rock interaction in supra-subduction zones remain poorly understood. Many microstructures may be overprinted by plastic strain or re-equilibration at high temperatures. Subsequently, low-temperature serpentinization and ductile deformation tend to erase all the pristine and intricate microstructures of melt-rock interaction. Consequently, studies focusing on the details of melt-rock interaction are limited (e.g., Piccardo et al., 2007; Rampone et al., 2008; Seyler et al., 2007; Suhr et al., 2008).

The tectonic setting of the Moa-Baracoa Ophiolitic Massif remains controversial. Some researchers interpret the massif as having formed in a back-arc basin due to the presence of upper pillow basalts with mid-oceanic ridge basalt-like (MORB-like) compositions (Marchesi et al., 2007). However, such an environment cannot adequately explain the harzburgites that have experienced high degrees (20%–30%) of partial melting (Marchesi et al., 2006). Some upper igneous rocks and lower mantle sections of ophiolitic massifs are generally decoupled in tectonic environments (e.g., the Gerf ophiolite, Egypt, Zimmer et al., 1995; Abdel-Karim et al., 2016). Recent studies show that MORB-like basaltic magmas can be produced during subduction initiation (Reagan et al., 2010; Shervais et al., 2019; Xiong et al., 2017a). Therefore, detailed

studies focused on the mantle rocks of the Moa-Baracoa Ophiolitic Massif are important to better constrain the tectonic environment. In particular, the harzburgites in the massif preserve a variety of pristine microstructures that are suitable for revealing the nature of melt-rock interaction.

This paper presents the petrography, microstructure, mineral chemistry, and whole-rock geochemistry of the Moa-Baracoa harzburgites. Our study delineates melt-rock interaction in a forearc mantle wedge during subduction initiation and sheds light on the mantle wedge heterogeneity in modal mineralogy and mineral chemistry.

2. Geological setting

The northward collision of the Caribbean plate with the North American plate (NOAM) in the latest Cretaceous to late Eocene resulted in the emplacement of the Cuban ophiolites, Northern Cuban Ophiolite Belt (NCOB) in the center west, and the Mayarí-Baracoa Ophiolite Belt (MBOB) in the east (Iturralde-Vinent et al., 2006; Proenza et al., 2018). The ophiolite belts stretch for more than 1000 km along the northern margin of Cuba (Fig. 1a). The NCOB and MBOB are composed of strongly faulted ultramafic, plutonic, volcanic, and subduction mélange complexes and constitute a component of the Cuban orogenic belt (e.g., Iturralde-Vinent et al., 2016).

The most significant tectonic units in the geology of eastern Cuba are the MBOB, Early to Late Cretaceous volcanic arc units, Early Cretaceous high-pressure (HP) subduction mélanges, late Cretaceous HP metasedimentary rocks (Asunción terrane), and the Late Cretaceous to Early

Table 1
Petrological data.

Sample	Ol (wt%)	3 σ	Opx (wt%)	3 σ	Cpx (wt%)	3 σ	Sp (wt%)	3 σ	Sum	T _{Ca-in-Opx} (°C) ^a	T _{Al/Cr-in-Opx} (°C) ^b	T _{Opx-Cpx} (°C) ^c	T _{Ol,Sp} (°C) ^d
17Y2	77.4	0.04	19.4	0.06	2.0	0.04	1.0	0.01	100	1041–1058	904–928	976–1044	714–727
17Y5	86.1	0.01	12.1	0.01	1.1	0.01	0.7	0.00	100	892–1021	854–966	939–1074	679–692
17Y6	71.6	0.04	24.8	0.06	2.7	0.03	0.8	0.01	100	985–1079	892–934	949–1111	671–713
17Y7	71.5	0.03	25.0	0.04	2.6	0.03	0.7	0.01	100	930–1075	841–890	1022–1063	711–740
17Y8	71.2	0.03	26.1	0.04	2.1	0.02	0.5	0.01	100	972–1113	876–943	973–1072	724–738
17Y15	82.4	0.01	14.7	0.01	1.9	0.01	0.9	0.00	100	985–1071	895–972	848–1117	619–658
17Y18	74.0	0.02	22.5	0.03	2.8	0.02	0.6	0.01	100	962–1073	830–920	838–1099	676–708
17Y19	75.4	0.02	20.8	0.03	2.9	0.02	0.8	0.01	100	988–1076	818–929	894–1048	678–700

^a Calculated with the Ca-in-orthopyroxene thermobarometer of Brey and Köhler (1990) at 1.5 GPa.

^b Calculated with the Al/Cr-in-orthopyroxene thermobarometer of Witt-Eickschen and Seck (1991).

^c Calculated with the orthopyroxene-clinopyroxene thermobarometer of Brey and Köhler (1990) at 1.5 GPa.

^d Calculated with the olivine-spinel thermobarometer of O'Neill and Wall (1987) at 1.5 GPa.

Paleocene synorogenic basin (Iturralde-Vinent et al., 2016; Proenza et al., 2018). The MBOB is separated by major fault zones into two individual thrust-bounded blocks, the Mayarí-Cristal Ophiolitic Massif to the west, and Moa-Baracoa Ophiolitic Massif (MBOM) to the east (Proenza et al., 2018). The MBOM is approximately 100-km long and 10–30-km wide and covers an area of approximately 1500 km². The MBOM is tectonically emplaced on subduction-related metamorphic complexes (Purial complex) hosting serpentinitic mélanges (e.g., Sierra del Convento and La Tinta) (Fig. 1b). These mélanges occur as bodies disconnected from the principal ophiolitic massifs and consists of a serpentinite matrix and embedded high-pressure tectonic blocks. They are derived from the MORB and document the subduction of oceanic and volcanic arc lithosphere since the early Cretaceous (e.g., Lázaro et al., 2016). The Güira de Jauco Amphibolite Complex (GJAC) has been interpreted as the metamorphic sole of the MBOM. The GJAC has a MORB-like protolith that is believed to have formed in a back-arc setting (Lázaro et al., 2014). The MBOM and the metamorphic complex were thrust over Cretaceous volcanic arc units (e.g., Quibiján and Morel formations), which display various geochemical signatures (e.g., tholeiitic, boninitic, and calc-alkaline) that suggest axial-arc, back-arc, and forearc settings during the Early to Late Cretaceous (Iturralde-Vinent et al., 2006; Marchesi et al., 2006, 2007).

The MBOM is primarily composed of harzburgite with subordinate dunite, a Moho transition zone (i.e., high-Al podiform chromitite, gabbro-sills, and impregnated dunite), and an overlay sequence of layered gabbro and pillow basalts (Morel Formation) (Fig. 1c). The layered gabbro is in tectonic contact with the lower mantle peridotite and the upper Morel Formation, which is Turonian-Coniacian in age and has a back-arc geochemical affinity (Marchesi et al., 2007) and a genetic link with cumulate gabbro (Marchesi et al., 2006). MBOM is generally considered to have formed in a back-arc environment based on the origins of the Morel Formation, the high-Al chromitite deposits, and the metamorphic sole (GJAC) (Gervilla et al., 2005; Marchesi et al., 2006, 2007; Zhou et al., 2001).

3. Analytical methods

Whole-rock major oxides were measured by X-ray fluorescence (XRF) on fused glass disks using a Shimadzu XRF-1800 instrument at the State Key Laboratory of Geological Processes and Mineral Resources, China University of Geosciences, Wuhan (GPMR-CUGW). Detailed analytical techniques are described in Lin et al. (2019). Two national standard materials (GBW07102 and GBW07112) were analyzed as unknowns together with the sample. Supplementary Table 1 shows the results. The analytical accuracy was within 3% for most elements.

Whole-rock trace elements and platinum-group elements (PGEs) were analyzed at the National Research Center for Geoanalysis, Chinese Academy of Geological Sciences (CAGS). Trace elements were determined using inductively coupled mass spectrometry (ICP-MS). The dissolution procedures of the samples were as follows. Sample powder,

HNO₃, and HF were added to a Teflon bomb. The Teflon bomb was placed in a stainless-steel pressure jacket and heated at 190 °C for >24 h then opened and evaporated to dryness on a hotplate at 140 °C. HNO₃ and MQ water were added, and the Teflon bomb was resealed and heated at 190 °C for >12 h. Two national standard samples (GBW07101 and GBW07102) were analyzed as unknowns; Supplementary Table 2 lists the results. The analytical accuracy was less than 10% for trace elements with abundances <10 ppm and approximately 5% for those with abundances >10 ppm. PGE concentrations were determined using the NiS fire-assay pre-concentration method, followed by ICP-MS analysis. Detailed analytical processes are described by Xiong et al. (2017b).

The major element compositions of the minerals were determined using a JEOL JXA-8530F Plus electron probe micro-analyzer (EPMA) at the Fundamental Science on Radioactive Geology and Exploration Technology Laboratory, East China University of Technology. EPMA analyses were performed at an accelerating voltage of 15 kV, a beam current of 20 nA, and a beam spot of 2 μm. The counting times were 10 s and 5 s for peak and background elements, respectively. Synthetic or natural mineral standards and a ZAF correction procedure were used for calibration. The relative standard deviations of the analyses on standards were within 1% for the major elements.

Trace element compositions of minerals were analyzed using a Teledyne Cetac Technologies Analyte Excite laser ablation coupled with an Agilent Technologies 7700× quadrupole inductively coupled plasma mass spectrometer (LA-ICP-MS) in GPMR-CUGW. For each analysis, laser ablation conditions of a spot size of 50 μm, pulse frequency of 10 Hz, and energy fluence of 4.5 J/cm² were applied. Background counting times were 25 s, followed by 45 s on the sample signal. NIST 610 was used to correct the time-dependent drift of the sensitivity. BCR-2G and BIR-1G were used as the external calibration standards. Offline data processing was conducted using the ICPMSDataCal software with 100% normalization without applying an internal standard (Liu et al., 2008). Supplementary Tables S9–12 present the results of the standards.

Electron backscattered diffraction (EBSD) analysis was performed using an Oxford Nordlys F+ EBSD detector attached to an FEI Quanta 450 SEM at the CAGS. Crystal orientation mappings were obtained at a voltage of 20 kV, a beam current of 180 μA, and step size of 4–10 μm. Automatic indexing was performed using Oxford Instruments AZtec software. The EBSD data were processed and optimized using HKL Channel 5 and MTEX. The orthogonal XYZ structural framework was coordinated using the crystallographic preferred orientation (CPO) of clinopyroxene. Detailed data processing was performed as described by Yang et al. (2019).

4. Petrography

The harzburgites studied were weakly to moderately altered. For each sample, modal compositions were calculated from the XRF and average EPMA data using least-squares regressions (Table 1). The Moa-Baracoa harzburgite is composed of olivine (Ol, 71%–86%) and

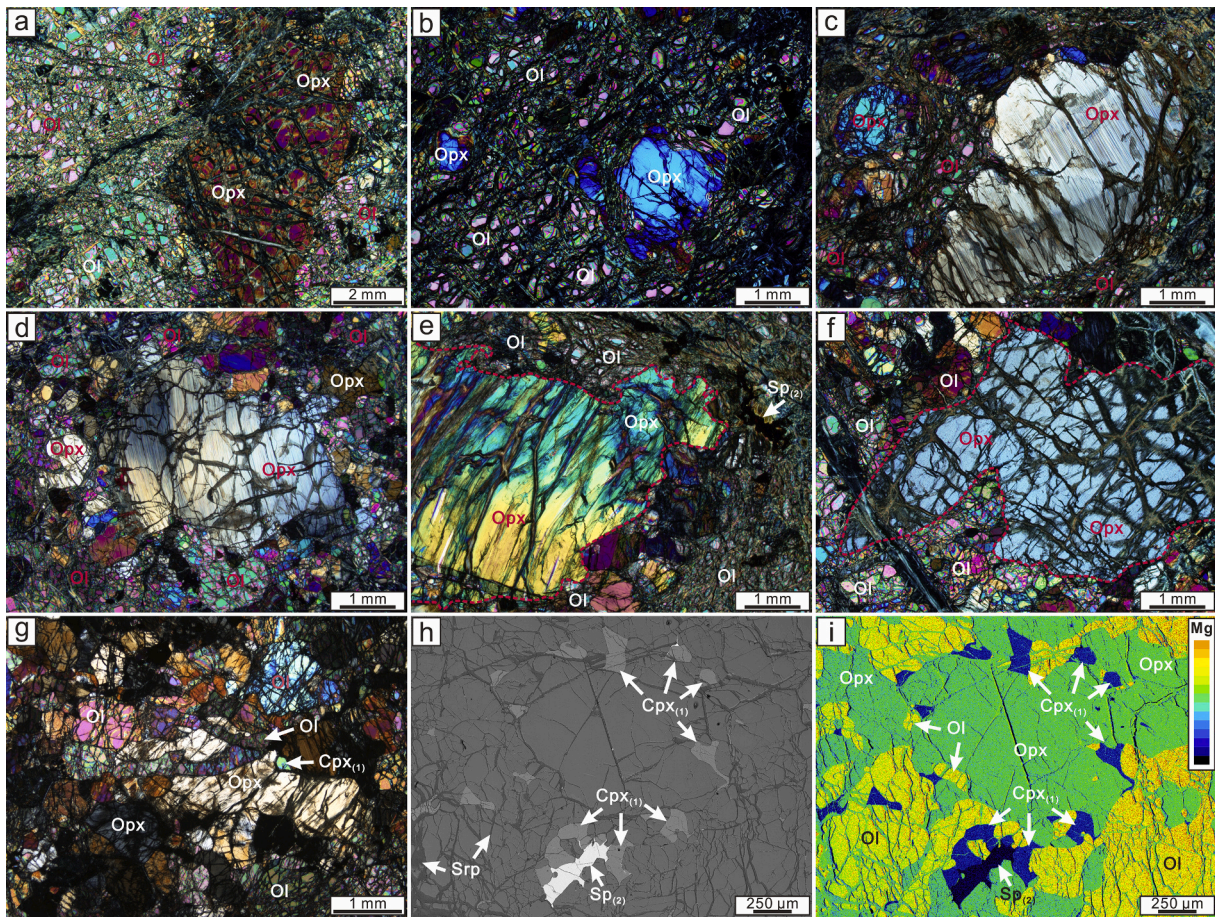


Fig. 2. Photomicrographs of the Moa-Baracoa harzburgites. (a, b) Harzburgites with porphyroclastic texture; (c, d) Kink bands in Opx porphyroclasts; (e, f) Opx embayed by fine-grained Ol neoblasts; (g) Aggregates of fine-grained Ol cut through Opx; (h) Cpx and Sp occur alongside boundaries of Opx (BSE image); (i) X-ray magnesium element mapping. Cpx: clinopyroxene, Ol: olivine, Opx: orthopyroxene, Serp: serpentine, Sp: spinel.

orthopyroxene (Opx, 12%–26%), with minor amounts of clinopyroxene (Cpx, 1%–3%), spinel (Sp, <1%), and base metal sulfides (BMS, <1%). The harzburgites display a typical porphyroclastic texture (Fig. 2a–b). Large orthopyroxene porphyroclasts show slight plastic deformation, such as kink bands and deformed lamellae exsolutions (Fig. 2c–d).

Most of the coarse-grained olivines were moderately broken, and their original grain sizes varied from 1 to 5 mm (Fig. 2a–b). Orthopyroxenes are subhedral to anhedral crystals with convex to concave outlines that tend to form aggregates of up to 10 mm in diameter. The orthopyroxene porphyroclasts are embayed by fine-grained olivine neoblasts smaller than 0.5 mm (Fig. 2e–f). Clinopyroxene occurs as irregular interstitial grains (Cpx₍₁₎) or as a matrix (Cpx₍₂₎) of symplectites. The Cpx₍₁₎ grain sizes range from 0.05 to 0.35 mm, commonly occur alongside the boundaries of orthopyroxene grains, and seemingly show a complementary outline with adjacent relic orthopyroxenes (Fig. 2g–h). Some clinopyroxene grains extend as interstitial films at the interface of Ol and Opx or fill fractures in Ol and Opx (Fig. 2h–i). In addition, scanning electron microscopy revealed occasional tiny lamellar exsolutions of orthopyroxene in Cpx₍₁₎. Cpx₍₁₎ and the exsolutions show no plastic deformation.

Spinel vary in shape, grain size, and texture. Residual spinels (Sp₍₁₎) are rounded crystals with sizes ranging from 0.5 to 2.0 mm and are randomly scattered in the silicate matrix. Serpentinized olivine relics are locally enclosed by Sp₍₁₎ (Fig. 3a). Interstitial spinels (Sp₍₂₎) occur as irregular grains with sizes of 0.1–0.5 mm and usually coexist with Cpx₍₁₎ (Fig. 3b–c, e). Symplectites (~0.1 mm) consist of a Cpx₍₂₎ matrix with vermicular spinel (Sp₍₃₎) and sometimes overgrow around Cpx₍₁₎ and Sp₍₂₎ (Fig. 3d–e). BMS occurs as anhedral interstitial grains (Fig. 3f–i) or

subhedral to anhedral inclusions in silicates (Fig. 3j). Some of the BMS coexisted with Sp (Fig. 3k), or enclosed in Sp (Fig. 3l). The primary BMS is predominated by pentlandite, which is partly or completely replaced by magnetite and/or heazlewoodite (Fig. 3h, k–l).

5. Results

5.1. Whole-rock geochemistry

5.1.1. Major and minor elements

Supplementary Table S1 lists the whole-rock major and minor element data. The studied harzburgites are weakly to moderately altered with LOI values of 7.87–11.86 wt%. All iron was converted to FeO and renormalized on an anhydrous basis using the total of the original analyses. After renormalization, the harzburgites contained low contents of SiO₂ (43.30–45.14 wt%), Al₂O₃ (0.21–0.81 wt%), CaO (0.41–1.03 wt%), and TiO₂ (~0.04 wt%), and high contents of MgO (44.40–47.11 wt%) (Fig. 4). LOI is strongly correlated with MgO, SiO₂, and CaO and a very weak correlation with FeO, TiO₂, and Al₂O₃ (Supplementary Fig. S1).

5.1.2. Trace elements and PGE

Supplementary Table S2 provides the whole-rock trace element data. The harzburgites are highly depleted in accordance with typically low concentrations of rare earth elements (REE) and trace elements. Total REE contents vary from 0.16–0.39 ppm and are distinctly lower than those of the primitive mantle (7.43 ppm). On the chondrite-normalized REE diagram, the harzburgites show “U”-shaped patterns ((La/Yb)_N =

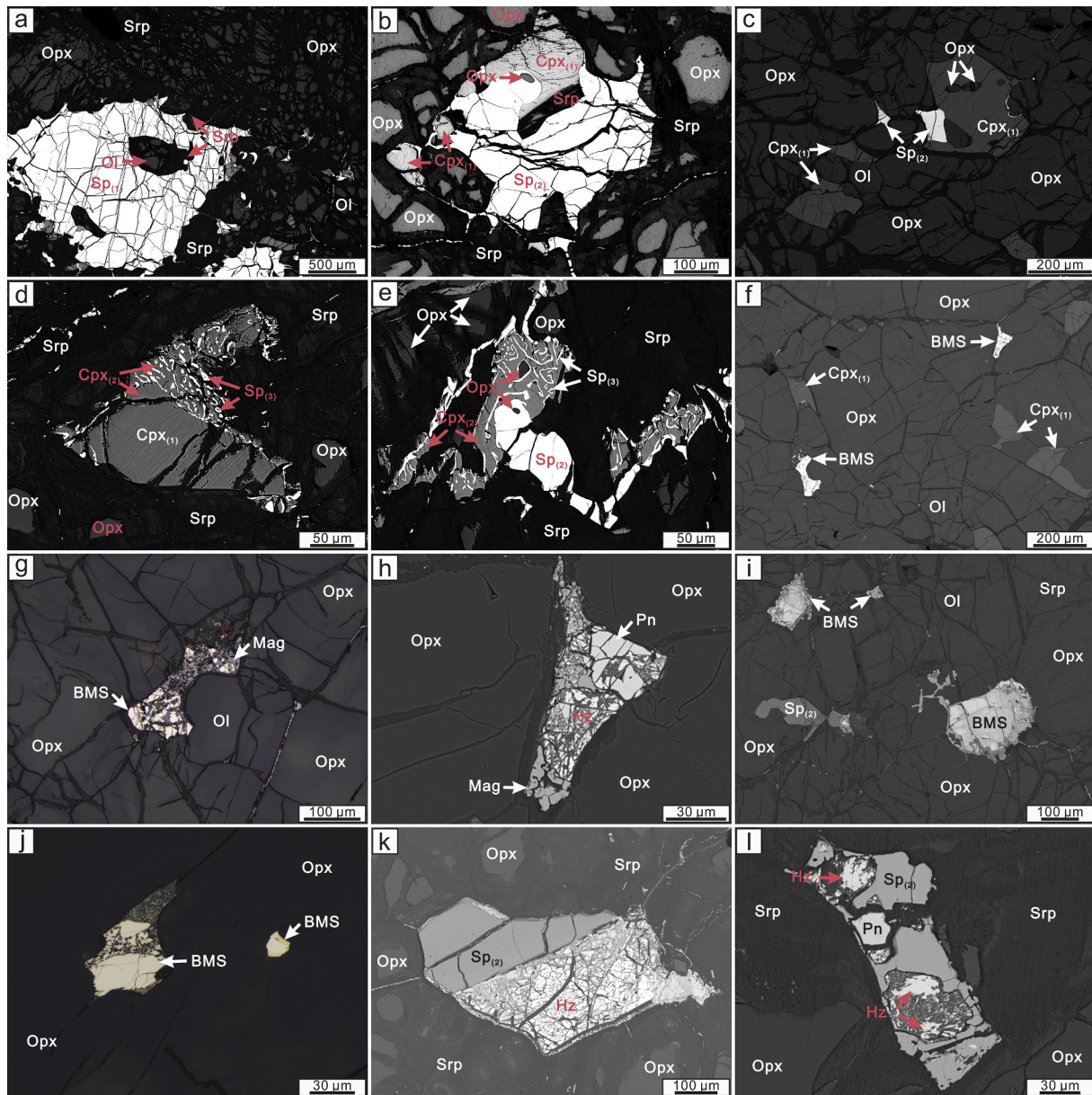


Fig. 3. Photomicrographs and back-scattered electron (BSE) images showing microstructures of the Moa-Baracoa harzburgites. (a) Serpentinized Ol relics enclosed by residual Sp; (b) Coexistence of interstitial Cpx and Sp; (c) Opx relics enclosed by interstitial Cpx; (d) Sp-Cpx symplectite overgrowth around interstitial Cpx; (e) Sp-Cpx symplectite overgrowth around interstitial Sp; (f) Interstitial Cpx and BMS; (g) BMS is partly replaced by Mag; (h) Pn is partly replaced by Mag and Hz; (i) Interstitial Sp and BMS; (j) BMS inclusions in Opx; (k) Coexistence of Sp and Hz; (l) Interstitial Sp encloses Pn and Hz. BMS: Base-metal sulfide, Cpx: clinopyroxene, Hz: Heazlewoodite, Mag: Magnetite, Ol: olivine, Opx: orthopyroxene, Pn: Pentlandite, Serp: serpentine, Sp: spinel.

0.50–2.55, $(La/Sm)_N = 1.94–4.70$) due to enrichment in light REE (LREE) and heavy REE (HREE) and depletion in middle REE (MREE) (Fig. 5a). Moreover, the harzburgites show positive anomalies in some large ion lithophile elements (LILE, e.g., Ba, U, and Sr) on the primitive mantle-normalized trace element diagram (Fig. 5b).

Supplementary Table S3 presents the whole-rock PGE data. The harzburgites have low PGE abundances ranging from 25.2–38.4 ppb. The chondrite-normalized PGE patterns plot slightly below the primitive mantle but within the spectrum of oceanic peridotite on the chondrite-normalized REE diagram (Fig. 6a). The fractionation between IPGE and PPG in harzburgite is very weak; the average values of $(Pd/Ir)_N$ (1.66) and $(Pd/Os)_N$ (1.43) are close to those of the primitive mantle (Fig. 6b).

5.2. Mineral chemistry

5.2.1. Major elements

Supplementary Tables S4–8 list the EPMA data. Coarse- and fine-grained olivines have high Fo values (90.6–91.6) and NiO contents (0.38–0.55 wt%) (Fig. 7a). Orthopyroxene porphyroclasts display compositional heterogeneity with similar Mg# values (91.0–92.2) and Al_2O_3 contents (1.20–2.10 wt%) but slightly lower CaO (0.63–1.84 wt%) and Cr_2O_3 (0.50–0.77 wt%) contents in the rims than in the cores (1.04–1.96 wt% and 0.60–0.87 wt%, respectively) (Fig. 7b–c). Interstitial Cpx has moderate Mg# values (92.1–94.6), Al_2O_3 contents (1.86–2.88 wt%), and Cr_2O_3 contents (0.82–1.22 wt%) and very low TiO_2 contents (<0.03 wt%) (Fig. 7d–f). The Cpx of the Sp-Cpx symplectites have higher Mg# values (92.7–94.9) and lower contents of Al_2O_3 (1.06–2.60 wt%), Cr_2O_3 (0.71–1.18 wt%), and TiO_2 (<0.02 wt%)

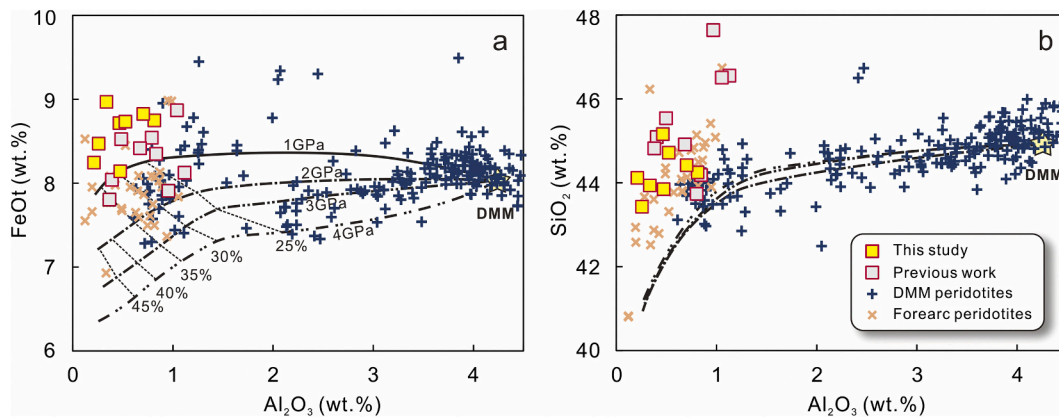


Fig. 4. Variation diagrams of whole-rock MgO (wt%) vs. FeOt (wt%) and SiO₂ (wt%) of the Moa-Baracoa harzburgites. Previous work data are from Marchesi et al. (2006). The data for DMM peridotites of Mongolia are from Carlson and Ionov (2019) and reference therein, forearc peridotite data are from Parkinson and Pearce (1998). Also shown are evolution trends for residues of anhydrous melting of DMM at 1–4 GPa (Herzberg, 2004).

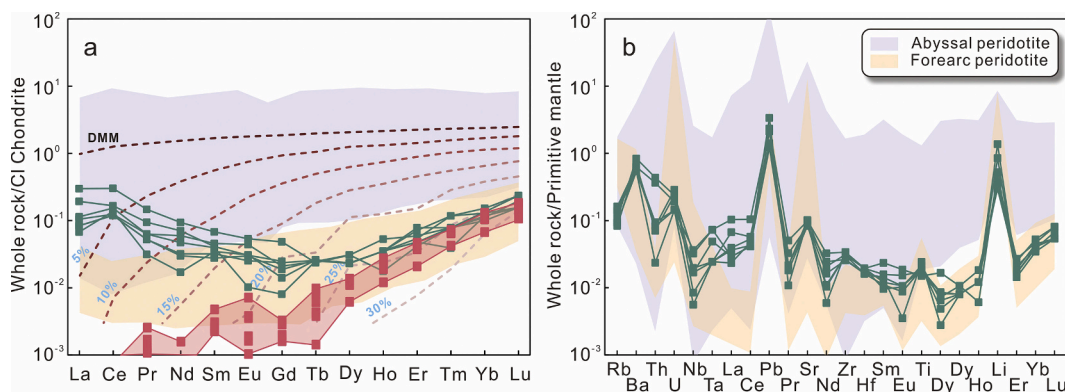


Fig. 5. (a) Chondrite-normalized measured (green) and recalculated (pink) REE patterns of the Moa-Baracoa harzburgites; (b) Primitive mantle-normalized trace elements diagram. Abyssal peridotite data are from Niu (1997). Forearc peridotite data are from Parkinson and Pearce (1998). Also shown are residue whole-rock HREE compositions calculated using the DMM source (Salters and Stracke, 2004) and nonmodal fractional melting equation of Gast (1968) and Johnson et al. (1990). (For interpretation of the references to colour in this figure legend, the reader is referred to the web version of this article.)

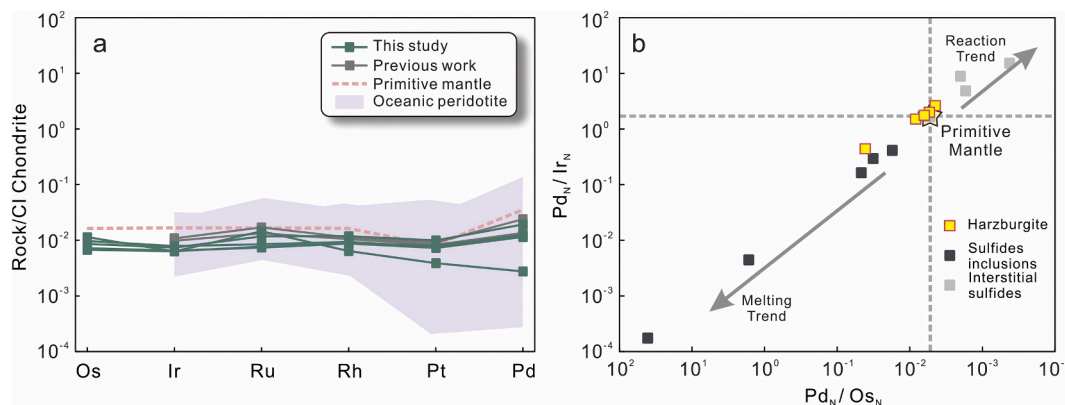


Fig. 6. (a) Chondrite-normalized PGE patterns of the Moa-Baracoa harzburgites; (b) Chondrite-normalized Pd_N/Ir_N vs. Pd_N/Os_N of the Moa-Baracoa harzburgites. Previous work data in (a) are from Zhou et al. (2001). Oceanic peridotite fields are from Marchesi et al. (2013). Data for the PGE contents of sulfide inclusions and interstitial sulfides and trends are from Alard et al. (2000).

than the interstitial Cpx (Fig. 7d–f).

Spinel compositions vary among the different microstructure sites (e. g., Sp₍₁₎, Sp₍₂₎, and Sp₍₃₎) but show no significant intra-grain zoning. Sp₍₁₎, Sp₍₂₎, and Sp₍₃₎ have constant Cr# values (56.7–64.8), but slowly decreasing Mg# values (52.1–58.4, 42.6–57.4, and 37.2–55.4, respectively) (Fig. 8).

The interstitial and enclosed pentlandites have consistent amounts of S (31.7–35.7 wt%), variable Fe (21.7–35.1 wt%), and Ni levels (31.3–45.3 wt%), similar to high-temperature monosulfide solid solutions (MSS) (Fig. 9). Heazlewoodites are characterized by high Ni levels (71.3–74.4 wt%) and relatively low S contents (26.1–27.9 wt%) (Fig. 9).

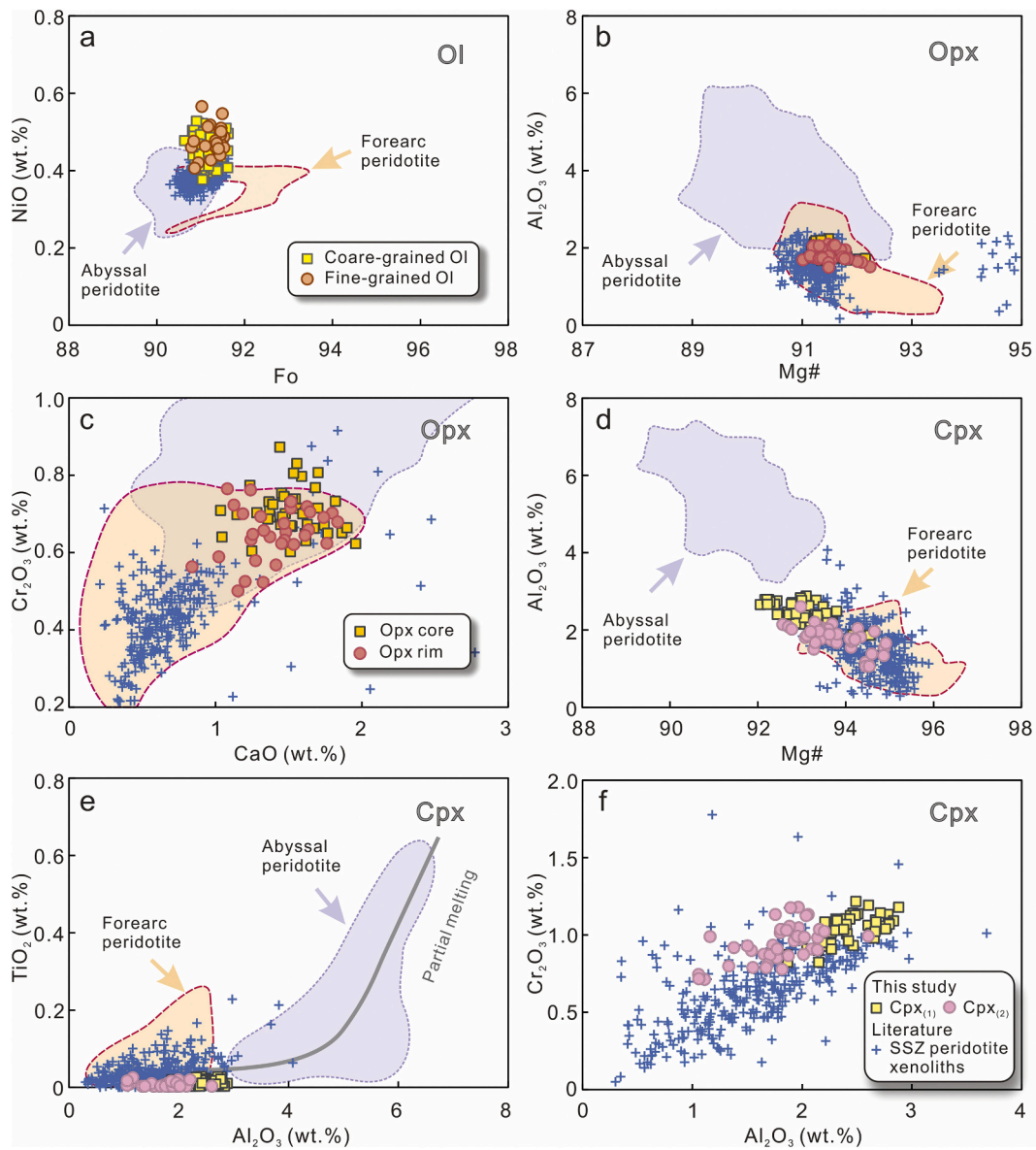


Fig. 7. Compositional variations of olivine, orthopyroxene, and clinopyroxene in the Moa-Baracoa harzburgites. The SSZ peridotite xenolith data are from [Bénard et al. \(2021\)](#). Abyssal and forearc peridotite fields are from [Lian et al. \(2017\)](#).

5.2.2. Trace elements

Supplementary Tables S9–12 provide the trace element compositions in olivine, orthopyroxene, clinopyroxene, and spinel. Opx and interstitial Cpx have low \sum REE values (0.09–0.14 and 0.24–0.49 ppm, respectively). Opx and Cpx show LREE-depleted patterns on the chondrite-normalized REE diagrams. Opx generally shows a more restricted range in REE than Cpx ([Fig. 10a, c](#)). In the primitive-normalized trace element diagrams, Opx and Cpx were variably enriched in LILE (e.g., Cs, Rb, Pb, and Sr ([Fig. 10b, d](#))). Residual spinels have slightly variable trace elements (Sc, Ti, V, Mn, Co, Ni, Zn, and Ga) between individual samples, and Ga concentrations (23–38 ppm) decreases as the Cr_2O_3 content increases ([Fig. 8d](#)).

5.3. Equilibrium temperatures

[Table 1](#) lists the estimated equilibrium temperatures using core compositions of coarse grains and assuming a pressure of 1.5 GPa. The Ca-in-Opx thermometer ([Brey and Köhler, 1990](#)) provides a temperature range of 892–1113 °C (average of 1020 ± 43 °C). The Opx-Cpx thermometer ([Brey and Köhler, 1990](#)) yields a wide temperature range of

838–1117 °C (average of 994 ± 95 °C). The Al/Cr-in Opx thermometer ([Witt-Eickchen and Seck, 1991](#)) returns temperatures of 818–972 °C (average of 888 ± 58 °C). The Ol-Sp thermometer gives relatively low temperatures of 619–740 °C (average of 688 ± 31 °C) ([O'Neill and Wall, 1987](#)).

5.4. Microstructures (EBSD mapping)

The microstructures of a representative harzburgite sample were determined using EBSD analysis. Coarse- and fine-grained olivines display similar weak misorientations relative to the mean orientation of each grain ([Fig. 11a–b](#)). Olivine, orthopyroxene, and clinopyroxene show strong crystallographic preferred orientation (CPO) ([Fig. 11c](#)). The olivines display a fabric characterized by a CPO pattern in (001)[100] (E-type) and have a J-index of 6.23 ([Fig. 11c](#)).

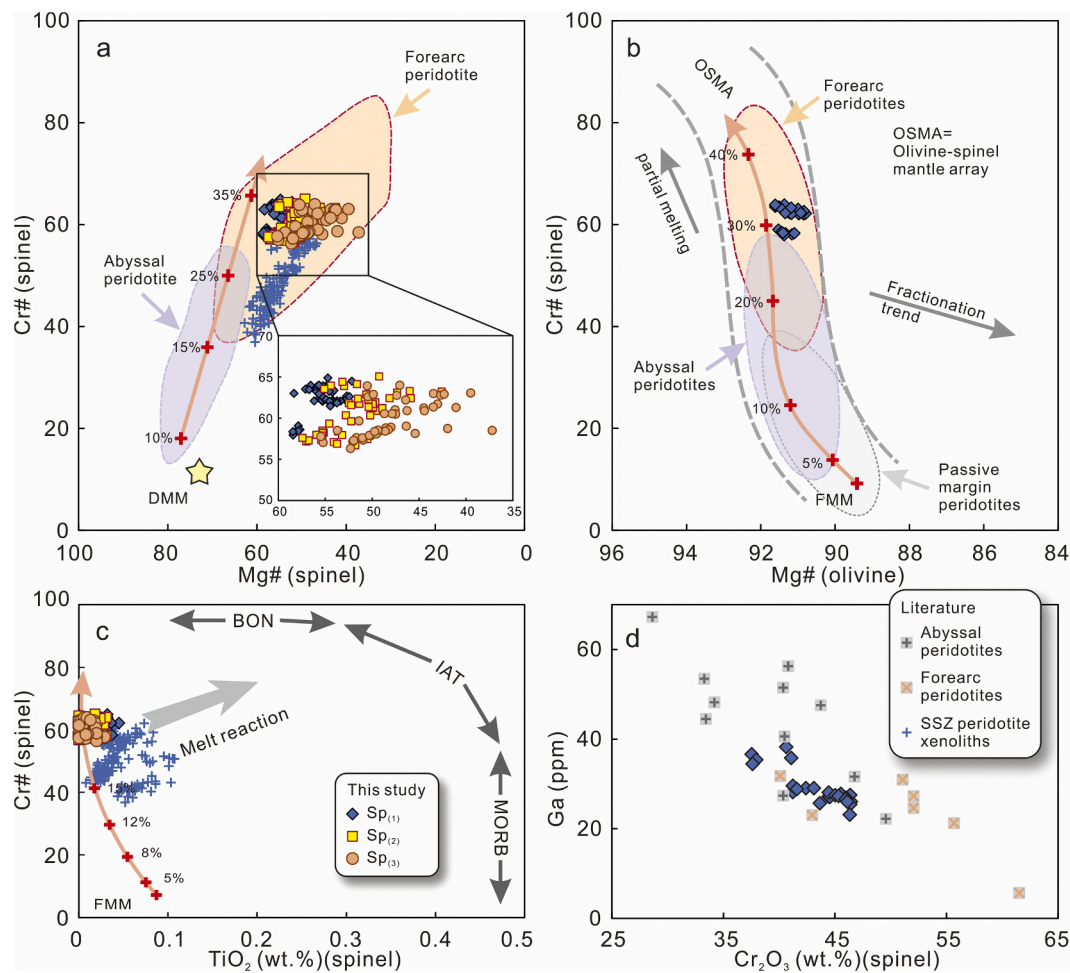


Fig. 8. Compositional variations of spinel in the Moa-Baracoa harzburgites. (a) Spinel Mg# vs. Cr# diagram. Abyssal and SSZ peridotite fields are from Dick and Bullen (1984) and Parkinson and Pearce (1998), respectively; (b) Olivine Mg# vs. spinel Cr#. Passive margin, abyssal, and SSZ peridotite fields and trends are from Pearce et al. (2000); (c) Spinel TiO₂ vs. Cr# diagram; (d) Spinel Cr₂O₃ (wt%) vs. Ga (ppm) diagram. SSZ peridotite xenolith data are from Bénard et al. (2021). The data for abyssal and forearc peridotites in (d) are from Dare et al. (2009).

6. Discussion

6.1. Partial melting processes

Despite strong or weak correlations between LOI and anhydrous oxides (Supplementary Fig. S1), the Moa-Baracoa harzburgites have relatively high FeOt and SiO₂ contents that resemble dredged forearc peridotites (Fig. 4). Marchesi et al. (2006) suggested that the Moa-Baracoa harzburgites experienced a high degree (20%–30%) of partial melting. In this study, the modal mineralogy, mineral chemistry, and whole-rock compositions of the harzburgites provide effective constraints on the partial melting degrees. The harzburgites predominantly consist of olivine and orthopyroxene with minor secondary clinopyroxene. The absence of primary clinopyroxene and the relatively high levels of olivine Fo and high spinel Cr# (Fig. 8b) indicate that the Moa-Baracoa harzburgites are residues of a high degree of partial melting.

Furthermore, the whole-rock HREE of mantle peridotites is correlated with the degree of partial melting (Johnson et al., 1990). In this study, HREE concentrations were not correlated with LOI (Supplementary Fig. S1) and were, therefore, immobile elements during peridotite serpentinization. Residue whole-rock HREE compositions were calculated using the DMM source (Salters and Stracke, 2004) and the non-modal fractional melting equation of Gast (1968) and Johnson et al. (1990). The results are displayed in a normalized pattern (Fig. 5a). To eliminate serpentinization and intergranular material effects, whole-

rock REE concentrations were recalculated using mineral modal compositions and in situ REE data (e.g., Bénard et al., 2021). The measured and recalculated HREE patterns of the Moa-Baracoa harzburgites were well modeled by >25% partial melting occurring in the spinel stability fields (Fig. 5a).

High partial melting was also observed in the microstructures. Orthopyroxene porphyroclasts have corroded or skeletal appearances and commonly contain fine-grained olivine neoblasts in the Moa-Baracoa harzburgites (Fig. 2e–f), suggesting that orthopyroxene was replaced by olivine. Similar microstructures are widely documented in abyssal peridotites (Dijkstra et al., 2003; Seyler et al., 2007), ophiolitic peridotites (Rampone et al., 2008; Xu et al., 2021), and anhydrous partial melting experiments (e.g., Kinzler, 1997) and are ascribed to the incongruent melting of orthopyroxene during asthenospheric upwelling and decompression (Niu, 1997; Rampone et al., 2008). This process is effectively enhanced by adiabatically ascending melts (Kelemen, 1990; Rampone et al., 2008; Seyler et al., 2007; Suhr et al., 2008).

On the one hand, fine-grained olivine aggregations cutting orthopyroxene relics (Fig. 2g) in the Moa-Baracoa harzburgites might verify the involvement of incongruent melting. On the other hand, E-type olivine fabrics generally develop under hydrous conditions (Harigane et al., 2013). Furthermore, residual spinels occasionally enclose small olivine relics as a result from continuous regrowth of spinel from melts. Suhr et al. (2008) proposed that Cr could reprecipitate around existing spinel after short-distance transport in melts and form coarse spinel in

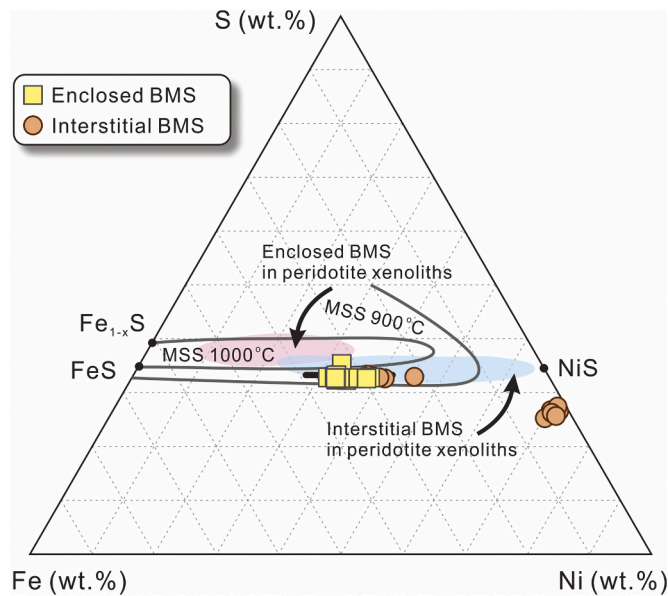


Fig. 9. Compositional variations of the Moa-Baracoa BMS in the Fe-Ni-S system. MSS compositional ranges are after [Craig and Kullerud \(1969\)](#). Fields of enclosed and interstitial BMS in peridotite xenoliths are from [Lorand and Luguet \(2016\)](#).

peridotites due to limited Cr mobility during melting. Low-Si melts traveling upward at adiabatic temperatures are the best candidates for enhancing incongruent melting, because they tend to dissolve enclosing peridotites; this saturates the melts with olivine but not with

orthopyroxene ([Kelemen et al., 1995](#)). Therefore, we infer that migrating low-Si mantle melt facilitated partial melting and the development of E-type olivine fabric.

6.2. Interaction of refractory harzburgites with melts

6.2.1. Origins of Cpx and BMS

Interstitial Cpx, Sp, and BMS are widespread in the Moa-Baracoa harzburgites. However, the occurrence of Cpx and BMS is inconsistent with the highly refractory nature of harzburgites subjected to >25% partial melting. Interstitial Cpx and Sp commonly occur alongside the boundaries of orthopyroxene grains and seemingly show a complementary outline with adjacent orthopyroxene porphyroclasts ([Fig. 2g-i](#)). Locally, small orthopyroxene relics are completely enclosed by interstitial Cpx or Sp ([Fig. 3b-c](#)). The interstitial Cpx and Sp are similar to those formed during melt-rock interaction (e.g., [Suhr et al., 2008](#)) and show microstructures that suggest the interaction of porous melts with peridotites, in which Cpx and Sp crystallized at the expense of orthopyroxene. Moreover, Cpx and Opx were enriched in LILE ([Fig. 10](#)), resembling those modified by cryptic metasomatism in peridotite xenoliths ([Bénard et al., 2021](#)).

The consumption of Opx and the precipitation of Cpx and Sp require a Ca- and Cr-rich low-Si melt saturated with Cr and precipitated Sp while cooling. Thus, the Si content in the residual melt increases slightly ([Suhr et al., 2008](#)). High concentrations of Si and Cr also suppress Al activity, which increases the stability of clinopyroxene ([Liu and O'Neill, 2004](#)) and triggers precipitation of interstitial Cpx ([Suhr et al., 2008](#)).

The occurrence of BMS is closely associated with interstitial Sp. Some of the BMS coexisted with Sp or enclosed in Sp ([Fig. 3k-l](#)). Primary BMS is predominantly composed of pentlandites. Compositional similarities with high-temperature MSS ([Fig. 9](#)) indicate the origin of sub-solidus

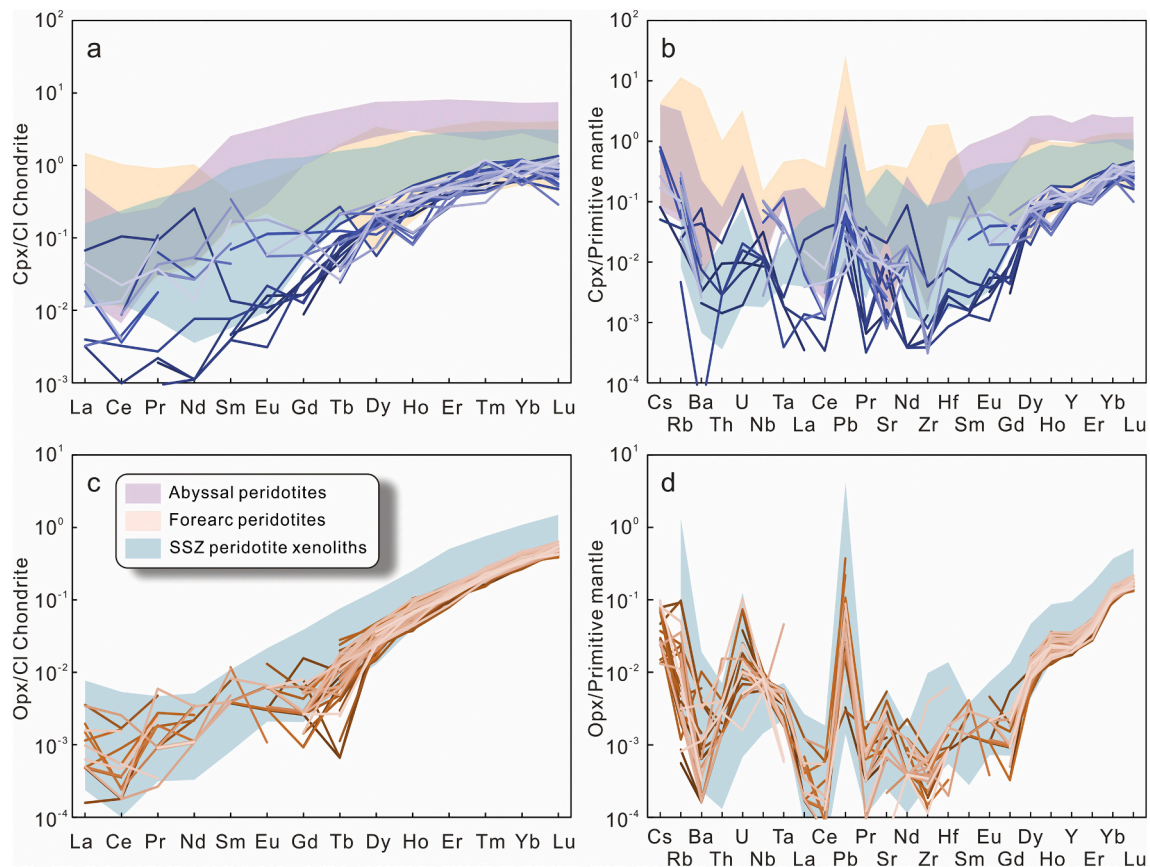


Fig. 10. (a, c) Chondrite-normalized REE patterns of clinopyroxene and orthopyroxene in the Moa-Baracoa harzburgites; (b, d) Primitive mantle-normalized trace elements diagrams. The data for abyssal and forearc peridotites are from [Uysal et al. \(2012\)](#); data for SSZ peridotite xenoliths are from [Bénard et al. \(2021\)](#).

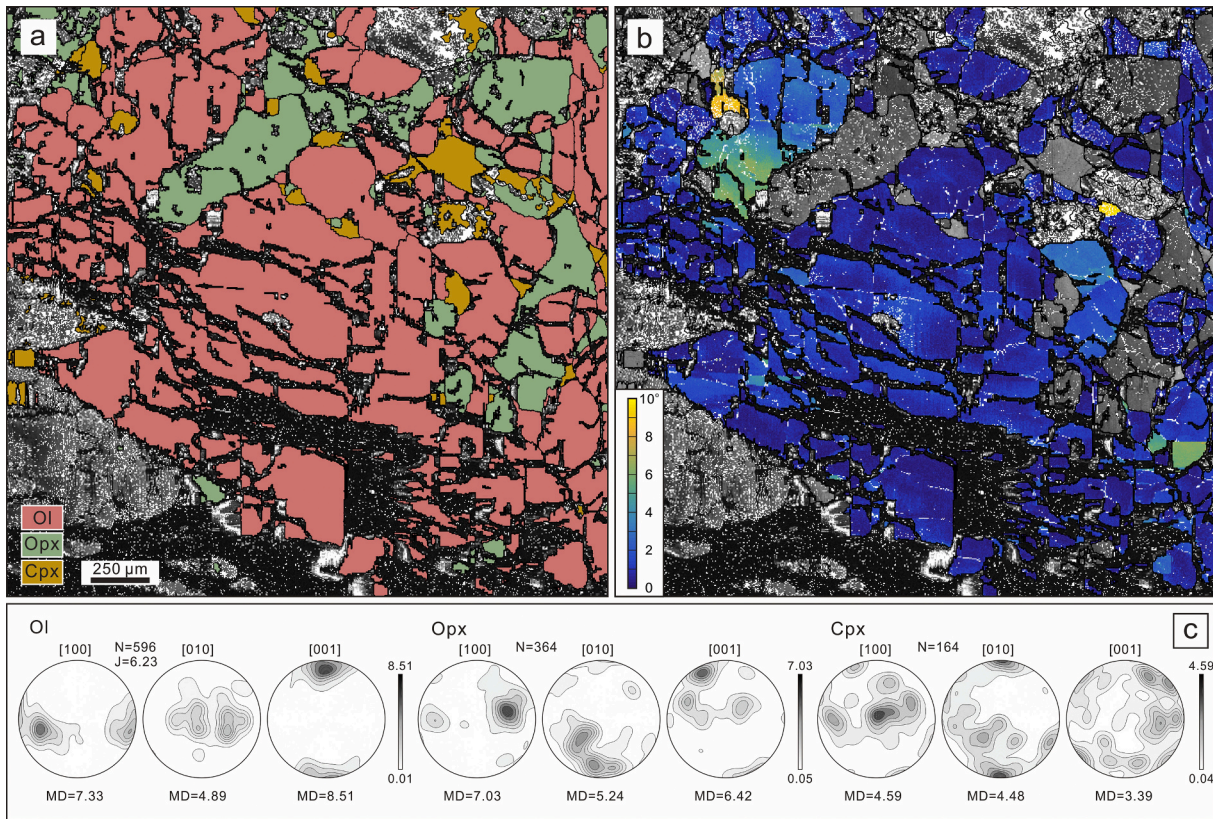


Fig. 11. (a) Phase distribution map of a representative harzburgite; (b) EBSD misorientation maps relative to the mean orientation of each grain; (c) Pole figures for the crystallographic axes of olivine, orthopyroxene, and clinopyroxene.

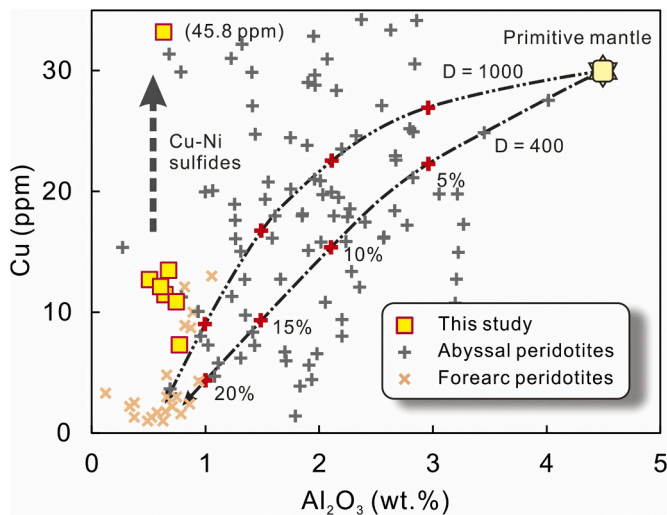


Fig. 12. Whole-rock Al_2O_3 vs. Cu of the Moa-Baracoa harzburgites. Abyssal peridotites data are from Niu (1997). Forearc peridotites data are from Parkinson and Pearce (1998). Also shown are evolution trends for residues of melting models based on different partition coefficients (D) (Marchesi et al., 2013).

MSS cooling. Theoretically, BMS completely disappears from residual mantle after ~12%–20% partial melting of a fertile mantle (e.g., Luguet et al., 2003). Sulfide separation from or input into the upper mantle chiefly controls the chalcophile element concentrations of mantle residues (Bockrath et al., 2004). The occurrence of widespread magmatic BMS is consistent with the enrichment of whole-rock Cu concentrations (11–46 ppm) that deviate from the melting trend (Fig. 12).

This may also be related to PGE behavior. Hydrothermal processes (e.g., serpentinization) have little impact on the magmatic PPGE budgets of peridotites (Pan and Wood, 1994). PGE concentrations in mantle peridotite are primarily controlled by partial melting and melt-rock interactions. Pt and Pd are highly depleted, whereas Os and Ir are relatively enriched in mantle residue during partial melting (Brenan et al., 2003). Pd/Ir ratios could indicate the degree of partial melting (e.g., Wu et al., 2019), because interstitial sulfides (rich in Pd) are easily melted (Woodland et al., 2002). Thus, Pd_N/Os_N and Pd_N/Ir_N ratios lower than PM are expected in the Moa-Baracoa harzburgites due to their high degree of partial melting. However, the PGE concentrations of the Moa-Baracoa harzburgites were considerably enriched in Pd and did not follow the melting trend (Fig. 6b).

Collectively, the textures and compositions of BMS and the significant enrichments of whole-rock Pd and Cu indicate that the primary BMSs were produced by the interaction of the refractory Moa-Baracoa harzburgites with S-saturated melt.

6.2.2. Nature of migrating melts

Researchers infer that the interaction between porous melts and plagioclase-free peridotites mostly occurs in the thermal boundary layer (TBL) or the lithospheric mantle (e.g., Dijkstra et al., 2003; Rampone et al., 2008; Seyler et al., 2001; Suhr et al., 2008). Additionally, decompression partial melting ceases when peridotites are incorporated into TBL, and post-melting refertilization or interaction between ascending buoyant melts and ambient peridotites inevitably occurs in TBL (Niu, 1997). Seyler et al. (2007) observed crystallization of clinopyroxene at the expense of orthopyroxene accompanied by precipitation of BMS and proposed that the interactions were promoted by rapid temperature decreases at relatively high pressure (~0.8–1 GPa) in the TBL. This is because the solubility of sulfur in the percolating melt decreases with increasing pressure or decreasing temperature (Naldrett,

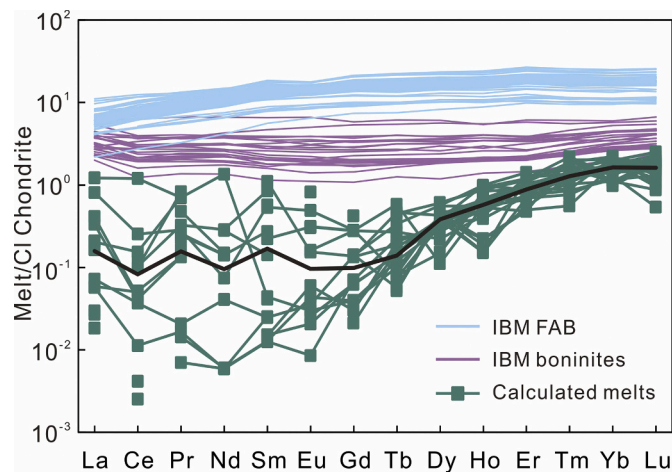


Fig. 13. Calculated composition of melts equilibrated with clinopyroxene. IBM boninite and FAB data are from Li et al. (2013) and Shervais et al. (2019), respectively.

1989).

Different hypotheses concerning the melt sources of reactive porous flow occurring in TBL have been proposed. The melts could be single increments originating from partial melting of the depleted mantle at shallow depths (i.e., upper pressure spectrum of the spinel stability field or above) beneath a spreading ridge (Basch et al., 2019; Seyler et al., 2001) or new ascending melts produced by decompression melting of the asthenosphere (Piccardo et al., 2007; Rampone et al., 2008). Percolate melts originating from different sources may have different compositions and lead to the precipitation of different mineral assemblages. Partial melting of the shallow mantle generally produces low-pressure Si-rich melts that react with ambient peridotites, leading to orthopyroxene saturation (Kelemen et al., 1995) and the formation of abundant low-CaO orthopyroxene (<0.8%; Barth et al., 2003; Bénard et al., 2021). In contrast, high-pressure melt fractions are driven to clinopyroxene saturation during the dissolution of enclosing peridotites and precipitation of olivines (Dijkstra et al., 2003; Kelemen et al., 1995). Mitchell and Grove (2016) recently conducted systemic experiments to simulate the interaction of high-pressure hydrous melts with the shallow-depleted mantle in the upper mantle wedge. The high-pressure (1.6 GPa) mantle melts reacted with shallow depleted peridotite at 1.2 GPa and produced very similar outcomes, namely consumption of orthopyroxene and precipitation of olivine, clinopyroxene, and spinel (Mitchell and Grove, 2016).

In the studied Moa-Baracoa harzburgites, crystallized mineral phases during melt-rock interaction were dominated by clinopyroxene, spinel, and BMS. Interstitial Cpx occasionally exsolves lamellar orthopyroxene, which is usually believed to transform from a high-PT predecessor (Xiong et al., 2019). The BMS originates from the sub-solidus cooling of high-T MSS. In addition, the overwhelming majority of orthopyroxenes have CaO contents of 1–2 wt% that are different from those formed by the interaction of peridotites with low-pressure Si-rich melts (Fig. 7c). Thus, we infer that the interaction of the Moa-Baracoa harzburgite with ascending low-Si melts occurred at the relatively high PT conditions of the lithospheric mantle.

Clinopyroxenes produced from the reaction of melt with orthopyroxene generally stabilize (Liu and O'Neill, 2004; Suhr et al., 2008), and their trace element compositions preserve important percolated melt signatures (e.g., Seyler et al., 2001, 2007). Therefore, we calculated the compositions of melts in equilibrium with $Cpx_{(1)}$ using the Cpx/melt partition coefficients proposed by Sun and Liang (2012). Fig. 13 shows the compositions of the calculated equilibrated melts plotted in a chondrite-normalized REE diagram. The melts are variably depleted in LREE and MREE relative to HREE, which is roughly consistent with

typical FAB (Fig. 13). However, the occurrence of BMS and enrichments of whole-rock PPGE and Cu requires an S-saturated melt, such as MORB or FAB. Moreover, the crust sequences (i.e., pillow basalt and layered gabbro) of the Moa-Baracoa Ophiolitic Massif have a MORB-like geochemical affinity (Marchesi et al., 2007). Therefore, we propose that the FAB melt is the best candidate for melt-rock interaction.

The melt/rock ratio is an important factor controlling the crystallizing assemblage and its proportion during melt-rock interaction (Mitchell and Grove, 2016). Experimental studies show that high melt volumes (>60%) react with harzburgites in the shallow mantle (0.5–1.0 GPa), produce abundant clinopyroxene, and crystallize wehrlite (Kelemen et al., 1990; Mitchell and Grove, 2016). However, clinopyroxene was not observed with very low melt volumes (5%) (Mitchell and Grove, 2016). The Moa-Baracoa harzburgites have very low clinopyroxene contents (1%–3%), implying relatively low melt/rock ratios in the melt-rock interaction.

6.3. Re-equilibration under low-PT conditions

The wide spectrum of equilibrium temperatures from 1020 to 688 °C indicates that the Moa-Baracoa harzburgites experienced subsolidus re-equilibration under low-PT conditions. Sp-Cpx symplectites also demonstrate subsolidus re-equilibration (Fig. 3d–e). Sp-Cpx symplectite refers to an intricate, texturally varied intergrowth of spinel and clinopyroxene that has been reported in the abyssal peridotite of the Mid-Atlantic Ridge (Seyler et al., 2001, 2007; Suhr et al., 2008) and in highly refractory peridotite of ophiolite (Dijkstra et al., 2010; Zhang et al., 2017; Zhou et al., 2021). These Sp-Cpx symplectites are significantly different from Sp-Opx-Cpx symplectite in mantle peridotite, which is interpreted as a pseudomorph of a pre-existing pyropic garnet formed by a phase transition from garnet to spinel-lherzolite (Gong et al., 2020).

Relatively lower temperatures are evidenced by the petrographic characteristics at this stage. For instance, orthopyroxene exsolution was not observed in the Cpx of the symplectite; thus, the symplectites unlikely formed and resided at high temperatures for an extended period. Additionally, symplectitic textures require limited diffusion, indicating a relatively low-temperature stage. Under such conditions, the solubility and diffusivity of Cr and other components can be effectively suppressed, leading to the formation of symplectites instead of isolated and separate spinel and clinopyroxene crystals (Suhr et al., 2008). Symplectite Cpx has higher Mg# but lower Al_2O_3 and Cr_2O_3 contents than interstitial Cpx (Fig. 7d). Sp in symplectite displays lower Mg# values than interstitial Sp (Fig. 8a). These chemical trends are consistent with the subsolidus Fe–Mg exchange between clinopyroxene and spinel and the decreased solubility of Cr–Al in pyroxene (Klemme and O'Neill, 2000) at decreasing temperatures. In addition, the decreasing trend of CaO and Cr_2O_3 contents from the core to the rim of the orthopyroxene (Fig. 7c) is consistent with long-term subsolidus equilibration and cooling (Ionov, 2010).

The symplectitic textures suggest the origin of the unmixing and cooling of high-PT pyroxenes. Rapidly cotectic precipitation of clinopyroxene and spinel from a melt also form similar textures (Seyler et al., 2007; Suhr et al., 2008). Sp-Cpx symplectite commonly overgrew the interstitial Sp and Cpx that formed during the melt-rock interaction. The mineral assemblage and close spatial relationship imply that the Sp-Cpx symplectite might be the result of re-equilibration of high-PT Cpx precipitated during melt-rock interaction.

6.4. Tectonic implication

Some researchers suggest that the MBOM formed in a back-arc basin since the upper pillow basalts (Morel Formation) and the layered gabbros have MORB-like compositions (Marchesi et al., 2007). Ophiolitic mantle peridotites also generally carry critical information and effectively constrain the tectonic settings in which they originated (e.g., Rui

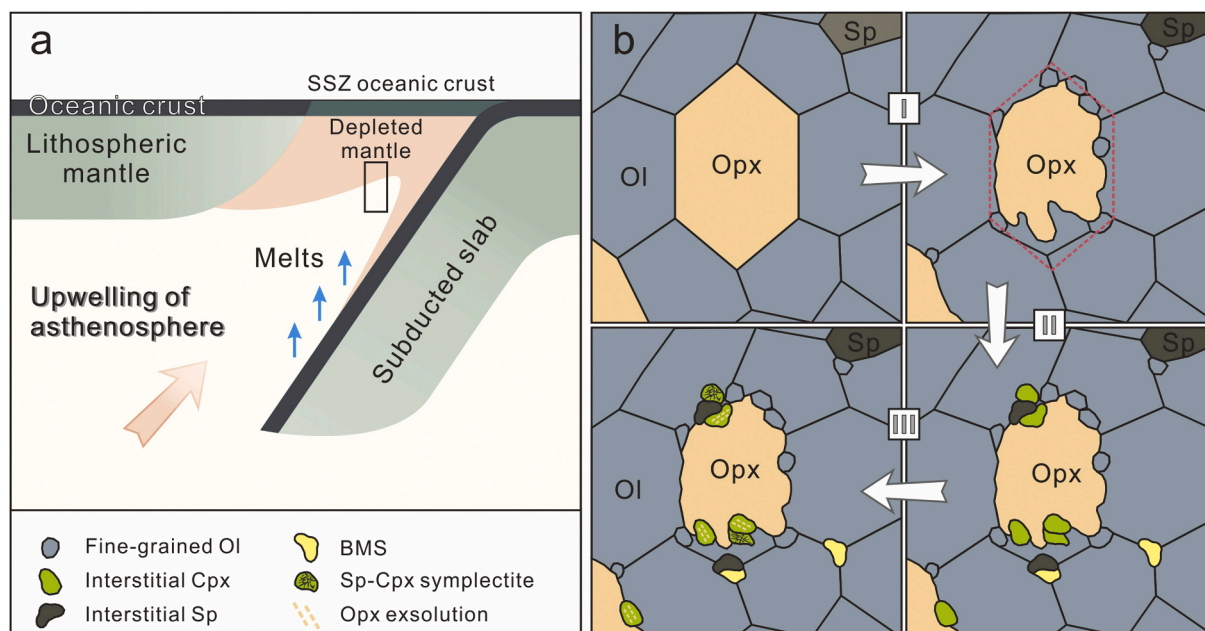


Fig. 14. Schematic cartoons (not to scale) illustrating the origin of the Moa-Baracoa harzburgites. I: Partial melting facilitated by melts; II: Interaction of refractory harzburgites with migrating FAB melts; III: Re-equilibration under low-PT conditions.

et al., 2019; Uysal et al., 2012; Yang et al., 2021).

The spinel Cr# and olivine Fo of peridotites systematically increased with increasing degrees of partial melting (Dick and Bullen, 1984). The Moa-Baracoa harzburgites plot within the fields of forearc peridotite on the Cr# (spinel) vs. Mg# (spinel) and Mg# (olivine) diagrams (Fig. 8a–b). Similarly, whole-rock major oxides and trace elements of the Moa-Baracoa harzburgites are analogous to forearc peridotites (Fig. 4–5).

Recent studies show that MORB-like basaltic magmas can be produced during subduction initiation (Lian et al., 2019; Reagan et al., 2010; Shervais et al., 2019; Wu et al., 2021; Xiong et al., 2017a). Here, we propose a subduction initiation environment to reconcile the MORB-like signatures of the Morel Formation (Marchesi et al., 2007) and the forearc affinities of the Moa-Baracoa harzburgites. A subduction initiation environment also favors the production of E-type olivine fabric (Harigane et al., 2013) in the Moa-Baracoa harzburgites. Moreover, a nascent forearc is the ideal tectonic setting for the generation of an FAB melt (e.g., Reagan et al., 2010; Xiong et al., 2017a) that reacted with refractory harzburgites in relatively high PT conditions and produced widespread Cpx and BMS.

The formation and preservation mechanisms of microstructures recording melt-rock interaction and re-equilibration of the Moa-Baracoa harzburgites may provide clues to the tectonic setting. It is ubiquitous that melt fractions travel by porous flow and lead to extensive melt-rock interaction in shallow mantle (e.g., Dijkstra et al., 2003; Warren, 2016). However, associated microstructures are rarely intactly and pristinely preserved in ophiolitic peridotites. Suhr et al. (2008) suggested that microstructures are best preserved when peridotites are frozen into a slow-spreading ridge with steeply dipping isotherms. In contrast, any such microstructure was probably erased by plastic strain in fast-spreading ridges with gently dipping isotherms (Suhr et al., 2008).

During subduction initiation, the upwelling asthenosphere cools as the cold slab descends into the warm mantle (e.g., Zheng, 2019); thus, a relatively steeply dipping thermal structure close to the cold slab can be produced. Therefore, we propose that the Moa-Baracoa harzburgites originated from a nascent forearc mantle wedge (Fig. 14) that experienced a high degree of partial melting, subsequent melt-rock interactions and re-equilibration, and repaid incorporation into the lithosphere during subduction initiation.

7. Conclusions

This study investigated the detailed melt-rock interaction that occurred in a nascent forearc mantle during subduction initiation. The Moa-Baracoa harzburgites contain widespread interstitial clinopyroxene, BMS, and an E-type olivine fabric. The primary BMS is predominated by pentlandite, which is partly or completely replaced by magnetite and/or heazlewoodite. The harzburgites preserve pristine microstructures that record partial melting, melt-rock interaction, and re-equilibration as the massif was rapidly emplaced into the lithospheric mantle during subduction zone initiation. The samples were subjected to a total of >25% partial melting. Migrating low-Si melts might have facilitated high degrees of partial melting and the development of olivine E-type fabrics. Subsequently, the interaction of the refractory harzburgites with ascending S-saturated and low-Si FAB melt at relatively high PT conditions precipitated interstitial clinopyroxene, spinel, and BMS. Finally, re-equilibration under low-PT conditions produced spinel-clinopyroxene symplectite. Our study suggests that melt-rock interaction is ubiquitous in nascent forearc mantle wedges that lead to mantle wedge heterogeneity in modal mineralogy and mineral chemistry. In addition, the enrichment of incompatible chalcophiles (i.e., Cu and Pt) in highly refractory mantle peridotites may result from interactions with ascending low-Si melts in the lithospheric mantle.

Supplementary data to this article can be found online at <https://doi.org/10.1016/j.lithos.2021.106427>.

Declaration of Competing Interest

The authors declare that they have no known competing financial interests or personal relationships that could have appeared to influence the work reported in this paper.

Acknowledgements

We thank Prof. A. C. Peña and Mrs. A. E. E. Borges for their assistance in the field. Drs. Guolin Guo and Jianbin Duan are appreciated for their assistance in EPMA analyses. Dr. Dongyang Lian is thanked for his suggestions and comments on earlier versions of the manuscript. Drs. Yu Yang and Chuqi Cao are grateful for the data processing. We thank the

reviewers for their constructive reviews, which have greatly improved the manuscript. This work was supported by grants from the Natural Science Foundation of China (41720104009, 92062215, 41802055, 41703053), the International Geoscience Programme (IGCP649, 2015–2020), and the Research Foundation from the Chinese Academy of Geological Sciences (J1903).

References

- Abdel-Karim, A.-A.M., Ali, S., Helmy, H.M., El-Shafei, S.A., 2016. A fore-arc setting of the Gerf ophiolite, Eastern Desert, Egypt: evidence from mineral chemistry and geochemistry of ultramafites. *Lithos* 263, 52–65.
- Abdullah, S., Misra, S., Ghosh, B., 2018. Melt-rock interaction and fractional crystallization in the Moho transition zone: evidence from the cretaceous Naga Hills Ophiolite, North-east India. *Lithos* 322, 197–211.
- Alard, O., Griffin, W.L., Lorand, J.P., Jackson, S.E., O'Reilly, S.Y., 2000. Non-chondritic distribution of the highly siderophile elements in mantle sulphides. *Nature* 407, 891–894.
- Barth, M.G., Mason, P.R.D., Davies, G.R., Dijkstra, A.H., Drury, M.R., 2003. Geochemistry of the Othris Ophiolite, Greece: evidence for refertilisation? *J. Petrol.* 44, 1759–1785.
- Basch, V., Rampone, E., Crispini, L., Ferrando, C., Ildefonse, B., Godard, M., 2019. Multi-stage reactive formation of troctolites in slow-spreading oceanic lithosphere (Erro-Tobbio, Italy): a combined field and petrochemical study. *J. Petrol.* 60, 873–906.
- Bénard, A., Müntener, O., Pilet, S., Arculus, R.J., Nebel, O., 2021. Silica-rich spinel harzburgite residues formed by fractional hybridization-melting of the intra-oceanic supra-subduction zone mantle: New evidence from TUBAF seamount peridotites. *Geochim. Cosmochim. Acta* 293, 477–506.
- Bockrath, C., Ballhaus, C., Holzheid, A., 2004. Fractionation of the platinum-group elements during mantle melting. *Science* 305 (1951–1955).
- Brenan, J.M., McDonough, W.F., Dalpe, C., 2003. Experimental constraints on the partitioning of rhenium and some platinum-group elements between olivine and silicate melt. *Earth Planet. Sci. Lett.* 212, 135–150.
- Brey, G.P., Köhler, T., 1990. Geothermobarometry in four-phase lherzolites II. New thermobarometers, and practical assessment of existing thermobarometers. *J. Petrol.* 31, 1353–1378.
- Carlson, R.W., Ionov, D.A., 2019. Compositional characteristics of the MORB mantle and bulk silicate earth based on spinel peridotites from the Tariat Region, Mongolia. *Geochim. Cosmochim. Acta* 257, 206–223.
- Craig, J.R., Kullerud, G., 1969. Phase relations in the Cu-Fe-Ni-S system and their applications to magmatic ore deposits. *Economic Geology Monograph* 4, 344–358.
- Dare, S.A.S., Pearce, J.A., McDonald, I., Styles, M.T., 2009. Tectonic discrimination of peridotites using f_{O_2} -Cr# and Ga-Ti-Fe^{III} systematics in chrome-spinel. *Chem. Geol.* 261, 199–216.
- Dick, H.J.B., Bullen, T., 1984. Chromian spinel as a petrogenetic indicator in abyssal and alpine-type peridotites and spatially associated lavas. *Contrib. Mineral. Petrol.* 86, 54–76.
- Dijkstra, A.H., Barth, M.G., Drury, M.R., Mason, P.R.D., Vissers, R.L.M., 2003. Diffuse porous melt flow and melt-rock reaction in the mantle lithosphere at a slow-spreading ridge: a structural petrology and LA-ICP-MS study of the Othris Peridotite Massif (Greece). *Geochemistry Geophysics Geosystems* 4, 8631.
- Dijkstra, A.H., Sergeev, D.S., Carl, S., Thomas, P., Thomas, M., Cawood, P.A., 2010. Highly refractory peridotites on Macquarie Island and the case for anciently depleted domains in the earth's mantle. *J. Petrol.* 51 (1–2), 469–493.
- Furnes, H., de Wit, M., Dilek, Y., 2014. Four billion years of ophiolites reveal secular trends in oceanic crust formation. *Geosci. Front.* 5, 571–603.
- Gast, P.W., 1968. Trace element fractionation and the origin of tholeiitic and alkaline magma types. *Geochim. Cosmochim. Acta* 32, 1057–1086.
- Gervilla, F., Proenza, J.A., Frei, R., González-Jiménez, J.M., Garrido, C.J., Melgarejo, J. C., Meibom, A., Díaz-Martínez, R., Lavaut, W., 2005. Distribution of platinum-group elements and Os isotopes in chromite ores from Mayarí-Baracoa Ophiolitic Belt (eastern Cuba). *Contrib. Mineral. Petrol.* 150, 589–607.
- Gong, X.H., Shi, R.D., Xu, J.F., Huang, Q.S., Huang, X.X., Su, B.X., 2020. "Garnet" lherzolites in the Purang ophiolite, Tibet: Evidence for exhumation of deep oceanic lithospheric mantle. *Geophysical Research Letters* 47. <https://doi.org/10.1029/2019GL086101>
- Harigane, Y., Michibayashi, K., Morishita, T., Tani, K., Dick, H.J.B., Ishizuka, O., 2013. The earliest mantle fabrics formed during subduction zone infancy. *Earth Planet. Sci. Lett.* 377–378, 106–113.
- Herzberg, C., 2004. Geodynamic information in peridotite petrology. *J. Petrol.* 45, 2507–2530.
- Ionov, D.A., 2010. Petrology of mantle wedge lithosphere: New data on supra-subduction zone peridotite xenoliths from the andesitic Avacha volcano, Kamchatka. *J. Petrol.* 51, 327–361.
- Iturralde-Vinent, M.A., Díaz-Otero, C., Rodríguez-Vega, A., Díaz-Martínez, R., 2006. Tectonic implications of paleontologic dating of Cretaceous-Danian sections of Eastern Cuba. *Geol. Acta* 4, 89–102.
- Iturralde-Vinent, M.A., García-Casco, A., Rojas-Agramonte, Y., Proenza, J.A., Murphy, J. B., Stern, R.J., 2016. The geology of Cuba: a brief overview and synthesis. *GSA Today* 26, 4–10.
- Johnson, K.T.M., Dick, H.J.B., Shimizu, N., 1990. Melting in the oceanic upper mantle: an ion microprobe study of diopsides in abyssal peridotites. *Journal of Geophysical Research: Solid Earth* 95, 2661–2678.
- Kelemen, P.B., 1990. Reaction between ultramafic rock and fractionating basaltic magma I. phase relations, the origin of calc-alkaline magma series, and the formation of discordant dunite. *J. Petrol.* 31, 51–98.
- Kelemen, P.B., Joyce, D.B., Webster, J.D., Holloway, J.R., 1990. Reaction between ultramafic rock and fractionating basaltic magma II. Experimental investigation of reaction between olivine tholeiite and harzburgite at 1150–1050°C and 5 kb. *J. Petrol.* 31, 99–134.
- Kelemen, P.B., Shimizu, N., Salters, V.J.M., 1995. Extraction of mid-ocean-ridge basalt from the upwelling mantle by focused flow of melt in dunite channels. *Nature* 375, 747–753.
- Kinzler, R.J., 1997. Melting of mantle peridotite at pressure approaching the spinel to garnet transition: Application to mid-ocean-ridge basalt petrogenesis. *J. Geophys. Res.* 102, 853–874.
- Klemme, S., O'Neill, H.S.C., 2000. The effect of Cr on the solubility of Al in orthopyroxene: experiments and thermodynamic modelling. *Contrib. Mineral. Petrol.* 140, 84–98.
- Lázaro, C., Blanco-Quintero, I.F., Proenza, J.A., Rojas-Agramonte, Y., Neubauer, F., Núñez-Cambra, K., García-Casco, A., 2016. Petrogenesis and ⁴⁰Ar/³⁹Ar dating of proto-forearc crust in the early cretaceous Caribbean arc: the La Tinta mélange (eastern Cuba) and its easterly correlation in Hispaniola. *Int. Geol. Rev.* 58, 1020–1040.
- Lázaro, C., García-Casco, A., Blanco-Quintero, I.F., Rojas-Agramonte, Y., Corsini, M., Proenza, J.A., 2014. Did the Turonian-Coniacian plume pulse trigger subduction initiation in the Northern Caribbean? Constraints from ⁴⁰Ar/³⁹Ar dating of the Moa-Baracoa metamorphic sole (eastern Cuba). *Int. Geol. Rev.* 57, 919–942.
- Li, Y., Kimura, J.L., Machida, S., Ishii, T., Ishiwatari, A., Maruyama, S., Qiu, H., Ishikawa, T., Kato, Y., Haraguchi, S., Takahata, N., Hirahara, Y., Miyazaki, T., 2013. High-Mg adakite and low-Ca boninite from a Bonin fore-arc seamount: Implications for the reaction between slab melts and depleted mantle. *J. Petrol.* 54, 1149–1175.
- Lian, D., Yang, J., Dilek, Y., Rocholl, A., 2019. Mineralogy and geochemistry of peridotites and chromitites in the Aladag Ophiolite (southern Turkey): Melt evolution of the cretaceous Neotethyan mantle. *J. Geol. Soc.* 176, 958–974.
- Lian, D., Yang, J., Liu, F., Wu, W., Zhang, L., Zhao, H., Huang, J., 2017. Geochemistry and tectonic significance of the Gongzhu peridotites in the northern branch of the western Yarlung Zangbo ophiolitic belt, western Tibet. *Mineral. Petrol.* 111, 729–746.
- Lin, A.B., Zheng, J.P., Xiong, Q., Aulbach, S., Lu, J.G., Pan, S.K., Dai, H.K., Zhang, H., 2019. A refined model for lithosphere evolution beneath the decratonized northeastern North China Craton. *Contrib. Mineral. Petrol.* 174 (2), 15.
- Liu, X., O'Neill, H., 2004. The effects of Cr₂O₃ on the partial melting of spinel lherzolite in the system CaO-MgO-Al₂O₃-SiO₂-Cr₂O₃ at 1.1 GPa. *J. Petrol.* 45, 2261–2286.
- Liu, Y.S., Hu, Z.C., Gao, S., Gunther, D., Xu, J.A., Gao, C.G., Chen, H.H., 2008. In-situ analysis of major and trace elements of anhydrous minerals by LA-ICPMS without applying an internal standard. *Chemical Geology* 257, 34–43.
- Lorand, J.P., Luguet, A., 2016. Chalcophile and siderophile elements in mantle rocks: Trace elements controlled by trace minerals. *Reviews in Mineralogy & Geochemistry* 81, 441–488.
- Luguet, A., Lorand, J.P., Seyler, M., 2003. A coupled study of sulphide petrology and highly siderophile element geochemistry in abyssal peridotites from the Kane Fracture Zone (Mark area, Mid-Atlantic Ridge). *Geochim. Cosmochim. Acta* 67, 1553–1570.
- Marchesi, C., Garrido, C.J., Bosch, D., Proenza, J.A., Gervilla, F., Monié, P., Rodríguez-Vega, A., 2007. Geochemistry of cretaceous magmatism in eastern Cuba: Recycling of north American continental sediments and implications for subduction polarity in the Greater Antilles Paleo-arc. *J. Petrol.* 48, 1813–1840.
- Marchesi, C., Garrido, C.J., Godard, M., Proenza, J.A., Gervilla, F., Blanco-Moreno, J., 2006. Petrogenesis of highly depleted peridotites and gabbroic rocks from the Mayarí-Baracoa Ophiolitic Belt (eastern Cuba). *Contrib. Mineral. Petrol.* 151, 717–736.
- Marchesi, C., Garrido, C.J., Harvey, J., González-Jiménez, J.M., Hidas, K., Lorand, J., Gervilla, F., 2013. Platinum-group elements, S, Se and Cu in highly depleted abyssal peridotites from the Mid-Atlantic Ocean Ridge (ODP Hole 1274A): Influence of hydrothermal and magmatic processes. *Contrib. Mineral. Petrol.* 166, 1521–1538.
- Mitchell, A.L., Grove, T.L., 2016. Experiments on melt-rock reaction in the shallow mantle wedge. *Contrib. Mineral. Petrol.* 171, 107. <https://doi.org/10.1007/s00410-016-1312-2>.
- Naldrett, A.J., 1989. Sulfide melts-crystallization temperatures, solubilities in silicate melts, and Fe, Ni, and Cu partitioning between basaltic magmas and olivine. In: Whitney, J.A., Naldrett, A.J. (Eds.), *Ore Depositions Associated with Magmas*. Review in Economic Geology, 4, pp. 5–20.
- Niu, Y.L., 1997. Mantle melting and melt extraction processes beneath ocean ridges: evidence from abyssal peridotites. *J. Petrol.* 38, 1047–1074.
- O'Neill, H.S.C., Wall, V.J., 1987. The olivine-orthopyroxene-spinel oxygen geothermometer, the nickel precipitation curve, and the oxygen fugacity of the Earth's upper mantle. *J. Petrol.* 28, 1169–1191.
- Pan, P., Wood, S.A., 1994. Solubility of Pt and Pd sulfides and Au metal in aqueous bisulfide solutions II. Results at 200° to 350°C and saturated vapor pressure. *Mineral. Deposita* 29, 373–390.
- Parkinson, I.J., Pearce, J.A., 1998. Peridotites from the Izu-Bonin-Mariana forearc (ODP Leg125): evidence for mantle melting and melt-mantle interaction in a suprasubduction zone setting. *J. Petrol.* 39, 1577–1618.
- Pearce, J.A., Baker, P.F., Edwards, S.J., Parkinson, I.J., Leat, P.T., 2000. Geochemistry and tectonic significance of peridotites from the South Sandwich arc-basin system, South Atlantic. *Contrib. Mineral. Petrol.* 139, 36–53.

- Piccardo, G.B., Zanetti, A., Poggi, E., Spagnolo, G., Müntener, O., 2007. Melt/peridotite interaction in the Southern Lanzo peridotites: Field, textural and geochemical evidence. *Lithos* 94, 181–209.
- Proenza, J.A., González-Jiménez, J.M., García-Casco, A., Belousova, E., Griffin, W.L., Talavera, C., Rogas-Agramonte, Y., Aiglsperger, T., Navarro-Ciurana, D., Pujol-Sola, N., Gervilla, F., O'Reilly, S.Y., Jacob, D.E., 2018. Cold plumes trigger contamination of oceanic mantle wedges with continental crust-derived sediments: evidence from chromitite zircon grains of eastern Cuban ophiolites. *Geosciences Frontiers* 9, 1921–1936.
- Rampone, E., Piccardo, G.B., Hofmann, A.W., 2008. Multi-stage melt-rock interaction in the Mt. Maggiore (Corsica, France) ophiolitic peridotites: Microstructural and geochemical evidence. *Contrib. Mineral. Petrol.* 156, 453–475.
- Reagan, M.K., Ishizuka, O., Stern, R.J., Kelley, K.A., Ohara, Y., Blichert-Toft, J., Bloomer, S.H., Cash, J., Fryer, P., Hanan, B.B., Hickey-Vargas, R., Ishii, T., Kimura, J. I., Peate, D.W., Rowe, M.C., Woods, M., 2010. Fore-arc basalts and subduction initiation in the Izu-Bonin-Mariana system. *Geochemistry Geophysics Geosystems* 11, Q03X12.
- Rui, H., Jiao, J., Xia, M., Yang, J., Xia, Z., 2019. Origin of chromitites in the Songshugou peridotite massif, Qinling Orogen (Central China): Mineralogical and geochemical evidence. *J. Earth Sci.* 30, 476–493.
- Salters, V.J.M., Stracke, A., 2004. Composition of the depleted mantle. *Geochemistry Geophysics Geosystems* 5, Q05B07.
- Seyler, M., Lorand, J.P., Dick, H.J.B., Drouin, M., 2007. Pervasive melt percolation reactions in ultra-depleted refractory harzburgites at the Mid-Atlantic Ridge, 15°20' N: ODP Hole 1274. *Contrib. Mineral. Petrol.* 153, 303–319.
- Seyler, M., Toplis, M.J., Lorand, J.P., Luguét, A., Cannat, M., 2001. Clinopyroxene microtextures reveal incompletely extracted melts in abyssal peridotites. *Geology* 29, 155–158.
- Shervais, J.W., Reagan, M., Haugen, E., Almeev, R.R., Pearce, J.A., Prytulak, J., Ryan, J. G., Whattam, S.A., Godard, M., Chapman, T., Li, H., Kurz, W., Nelson, W.R., Heaton, D., Kirchenbaur, M., Shimizu, K., Sakuyama, T., Li, Y., Vetter, S.K., 2019. Magmatic response to subduction initiation: part 1. Fore-arc basalts of the Izu-Bonin Arc from IODP expedition 352. *Geochemistry Geophysics Geosystems* 20, 314–338.
- Suhr, G., Kelemen, P., Paulick, H., 2008. Microstructures in Hole 1274A peridotites, ODP Leg 209, Mid-Atlantic Ridge: Tracking the fate of melts percolating in peridotite as the lithosphere is intercepted. *Geochemistry Geophysics Geosystems* 9, Q03012. <https://doi.org/10.1007/s004100050384>.
- Sun, C., Liang, Y., 2012. Distribution of REE between clinopyroxene and basaltic melt along a mantle adiabat: Effects of major element composition, water, and temperature. *Contrib. Mineral. Petrol.* 163, 807–823.
- Uysal, I., Ersoy, E.Y., Karsli, O., Dilek, Y., Burhan Sadiklar, M., Ottley, C.J., Tiepolo, M., Meisel, T., 2012. Coexistence of abyssal and ultra-depleted SSZ type mantle peridotites in a neo-Tethyan ophiolite in SW Turkey: Constraints from mineral composition, whole-rock geochemistry (major-rare-REE-PGE), and Re-Os isotope systematics. *Lithos* 132–133, 50–69.
- Warren, J.M., 2016. Global variations in abyssal peridotite compositions. *Lithos* 248–251, 193–219.
- Witt-Eickchen, G., Seck, H.A., 1991. Solubility of Ca and Al in orthopyroxene from spinel peridotite: an improved version of an empirical geothermometer. *Contrib. Mineral. Petrol.* 106, 431–439.
- Woodland, S.J., Pearson, D.G., Thirlwall, M.F., 2002. A platinum group element and Re-Os isotope investigation of siderophile element recycling in subduction zones: Comparison of Grenada, Lesser Antilles Arc, and the Izu-Bonin Arc. *J. Petrol.* 43, 171–198.
- Wu, W., Yang, J., Dilek, Y., Milushi, L., Lian, D., 2019. Multiple episodes of melting, depletion, and enrichment of the Tethyan mantle: Petrogenesis of the peridotites and chromitites in the Jurassic Skenderbeu massif, Mirdita ophiolite, Albania. *Lithosphere* 10, 54–78.
- Wu, W., Yang, J., Lian, D., Rui, H., 2021. New concepts in ophiolites, oceanic lithosphere and podiform chromites. In: Alderton, D., Elias, S.A. (Eds.), *Encyclopedia of Geology* (Second Edition). Academic Press, pp. 968–993.
- Xiong, F., Dilek, Y., Wirth, Richard, Xu, X., Yang, J., 2019. Opx-Cpx exsolution textures in lherzolites of the cretaceous Purang Ophiolite (S. Tibet, China), and the deep mantle origin of Neotethyan abyssal peridotites. *Int. Geol. Rev.* 62, 665–682.
- Xiong, F., Yang, J., Robinson, P.T., Xu, X., Liu, Z., Zhou, W., Feng, G., Xu, J., Li, J., Niu, X., 2017b. High-Al and high-Cr podiform chromitites from the western Yarlung-Zangbo suture zone, Tibet: Implications from mineralogy and geochemistry of chromian spinel, and platinum-group elements. *Ore Geol. Rev.* 80, 1020–1041.
- Xiong, Q., Henry, H., Griffin, W.L., Zheng, J., Satsukawa, T., Pearson, N.J., O'Reilly, S.Y., 2017a. High- and low-Cr chromitite and dunite in a Tibetan ophiolite: Evolution from mature subduction system to incipient forearc in the Neo-Tethyan Ocean. *Contrib. Mineral. Petrol.* 172, 45. <https://doi.org/10.1007/s00410-017-1364-y>.
- Xiong, Q., Xu, Y., González-Jiménez, J.M., Liu, J., Alard, O., Zheng, J., Griffin, W.L., O'Reilly, S.Y., 2020. Sulfide in dunite channels reflects long-distance reactive migration of mid-ocean-ridge melts from mantle source to crust: a Re-Os isotopic perspective. *Earth Planet. Sci. Lett.* 531, 115969.
- Xu, Y., Liu, C.Z., Lin, W., 2021. Melt extraction and reaction in the forearc mantle: Constraints from trace elements and isotope geochemistry of ultra-refractory peridotites of the New Caledonia Peridotite Nappe. *Lithos* 380–381, 105882.
- Yang, J.S., Wu, W.W., Lian, D.Y., Rui, H.C., 2021. Peridotites, chromitites and diamonds in ophiolites. *Nature Reviews Earth & Environment* 2, 198–212. <https://doi.org/10.1038/s43017-020-00138-4>.
- Yang, Y., Abart, R., Yang, X., Shang, Y., Ntaflou, T., Xu, B., 2019. Seismic anisotropy in the Tibetan lithosphere inferred from mantle xenoliths. *Earth Planet. Sci. Lett.* 515, 260–270.
- Zhang, C., Liu, C., Wu, F., Ji, W., Liu, T., Xu, Y., 2017. Ultra-refractory mantle domains in the Luqu ophiolite (Tibet): Petrology and tectonic setting. *Lithos* 286–287, 252–263.
- Zheng, Y., 2019. Subduction zone geochemistry. *Geosciences Frontiers* 10, 1223–1254.
- Zhou, M., Lewis, J., Malpas, J., Munoz-Gomez, N., 2001. The Mayari-Baracoa paired ophiolite belt, eastern Cuba: Implications for tectonic settings and platinum-group elemental mineralization. *Int. Geol. Rev.* 43, 494–507.
- Zhou, X., Zheng, J.P., Li, Y.B., Zhu, H., Griffin, W.L., O'Reilly, S.Y., 2021. Melt migration and interaction in a dunite channel system within oceanic forearc mantle: the Yushigou harzburgite–dunite associations, North Qilian Ophiolite (NW China). *J. Petrol.* <https://doi.org/10.1093/ptrology/egaa115>.
- Zimmer, M., Kroner, A., Jochum, K.P., Reischmann, T., Todt, W., 1995. The Gabal Gerf complex: a Precambrian N-MORB ophiolite in the Nubian Shield, NE Africa. *Chem. Geol.* 123, 29–51.